Two Fluid Model using Kinetic Theory for Modeling of One-Step Hydrogen Production Gasifier

Liang Yu and Jing Lu
State Key Lab of Multi-phase Complex Systems, Institute of Process Engineering, Chinese Academy of Sciences, Beijing, 100080, China

Graduate University of Chinese Academy of Sciences, 100049, Beijing, China

Xiangping Zhang and Suojiang Zhang
State Key Lab of Multi-phase Complex Systems, Institute of Process Engineering, Chinese Academy of Sciences, Beijing, 100080, China

Xiaoling Wang
Department of Mathematics, Zhengzhou University, Zhengzhou, 450052, China

DOI 10.1002/aic.11603
Published online October 6, 2008 in Wiley InterScience (www.interscience.wiley.com).

A Two Fluid Model (TFM) using kinetic theory of granular flow has been developed to describe an innovative process of hydrogen production in a single step. An extended Multi-species of Solid Phase (MSP) method is proposed to simulate the gas-solid heterogeneous reactions in an entrained flow gasifier, as opposed to Single-species of Solid Phase (SSP) in previous studies. The intrinsic equations of methane steam reforming and water-gas shift reactions are used for a good understanding of the reaction mechanism for high concentration of hydrogen production under higher pressure. On the basis of the results of computing, the main feature of core-annular reaction zone is predicted in the fully developed flow region. And the similar flame-like structure for velocity and temperature is observed to emerge from the feed injection zone at the bottom of gasifier. The model well illustrates the effects of CaO on enhancing the concentration of hydrogen and sequestering CO_2 in the process of coal gasification. The advantages of pressure gasification are also shown that coal conversion increases with increasing pressure while H_2S concentration and tar content decreases. Moreover, there is a steep increase in H_2S and tar species initiated from the entrance of gasifier and then a decrease at the next section. The model shows good agreement with the measurements of flow field and gas products concentration in laboratory-scale plants.
 AIChE J, 54: 2833–2851, 2008
Keywords: coal gasifier, two-fluid model, kinetic theory of granular flow

Introduction

Hydrogen as a clean energy source will greatly assist to reduce greenhouse effect and globe warming. Gasification-based systems such as Integrated Coal Gasification Combined

Correspondence concerning this article should be addressed to S. Zhang at sjzhang@home.ipe.ac.cn.

Cycle (IGCC) have been believed to have the potential capability of hydrogen production for concentrating and sequestering CO_2.[1] More attention has been paid to the process of hydrogen production from coal in a single step,[2–4] which combines the water gas shift reaction and reforming reactions with gasification in one reactor. This process can also be extended to biomass gasification and some excellent catalysts has been developed to accelerate a process of hydrogen and syngas production at very low temperature.[5–7] Although it is an energy-efficient and environmental friendly process, the design and optimization of reactor should be taken into account due to the complexity of integrating multi-step into one reactor. To understand the complicated physical and chemical phenomena occurring inside the reactor, mathematical modeling without cost-expensive and time-consuming test is the best learning tool.

In previous literatures, many mathematical models were developed for entrained flow gasifiers. There are three types of entrained flow gasifier models classified by the expression of momentum equation:

(1) Empirical models, where flow characteristic was not taken into account in gasifiers. Vamvuka et al.[8,9] assumed the two-phase flow to be one-dimensional with plug flow axially and complete radial mixing, so did Liu et al.[10] Fang et al.[11] divided the reactor into 80 short cylinder cells, and further divided each cell into four annular regions along the radial. In every annular region, gas and solid flow is assumed to be in plug flow. This assumption ignores the phenomenon of nonhomogeneous distribution of particles along the radial and axial coordinates of the riser.

(2) Eulerian-Largrangian models, where the governing gaseous fluid mechanics and reaction equations are solved in an Eulerian framework and the particle mechanics are solved by following representative individual particle trajectories in a Lagrangian frame of reference. On the basis of Eulerian-Largrangian framework, the Smoot's group develop the commercial code PCGC-2 and this code has been used to simulate several laboratory-scale gasifiers.[12–14] In stead of the Single Solid Progress Variable (SSPV), Chen et al.[15,16] extended gas mixture fraction model with the Multi Solid Progress Variables (MSPV) to simulate the gasification reaction and reactant mixing progress. Watanabe et al.[17] developed an evaluation technique for design and performance optimization of coal gasifiers and the validity of the model was confirmed. However, in the studies aforementioned, there are large memory requirements and long calculation time because each particle is tracked individually.[18–20]

(3) Eulerian-Eulerian models, where gas phase models and solid phase models are solved in an Eulerian framework. Govind et al.[21] used Arastoopour and Gidaspow's[22] early hydrodynamic model to simulate an one-dimensional steady-state entrained-bed pilot-plant gasification system. With the development of Two Fluid Model (TFM), more detailed coal particle processes can be described,[23] including particle drag and turbulent dispersion, heat-up, volatilization, drying and heterogeneous combustion. However, for ignoring the effect of the solid viscosity and the solid stress, thus the main features of the gas-solid flow pattern in the vertical pipe, such as the core-annular flow regime,[24] could not be described.

Among these three types of entrained flow gasifier models, TFM is more convenient to obtain the mean particulate flow fields which can facilitate quantifiable decisions for an engineering design.[25–27] Especially by means of introducing Kinetic Theory of Granular Flow (KTGF) into TFM, the core-annular structure in risers (vertical pipes) verified by oil industry can be predicted.[28–29]

With significant applications of KTGF, great progresses have been made to predict flow field of the fluidized beds in the past decade. By analogy with the idea gas law, Gidaspow et al.[30] thought that there exists an equation of state for particles in dilute flow. Mathiesen et al.[31] used KTGF to model the flow pattern of different particle sizes in the riser of a cold-flow circulating fluidized bed. Applying KTGF to gas-solid fluidized beds containing a mixture of two particle species, van Wachem et al.[18,19] developed TFM to consider a binary mixture of smooth, nearly elastic, spheres and to demonstrate key features of binary mixture fluidization. Furthermore, KTGF was also used to study the effects of particle size and density on particle interaction and overall behavior of granular flow.[32]

Although TFM using KTGF has given a reasonable flow description of riser and CFB, it is difficult that the complicated chemical reactions are introduced to simulate the gasification process. This is because complex mechanism of heat transfer and chemical reaction need to be modeled. More careful consideration has to be given on the solution of large numbers of energy and species transport equations and the nonlinear source term of complicated chemical reactions. Until now, not much effort has been devoted to integrate KTGF with complicated chemical reaction, especially hydrogen production in a single step. However, the scale-up and optimal design of industrial reactors can not be carried out without considering chemical reaction.

In the previous simulations of coal or biomass gasification, the second species of solid phase, such as limestone or sand, is ignored. This is because the second species of solid phase has little effect on the gas products. For example, in the traditional gasifier, the function of limestone is desulphurized, the content of sulfur is much less than that of the other species, thus in the process of simulation, the limestone is usually neglected. Many research groups[33–35] established gasification models called Single-species of Solid Phase (SSP) method, only including char species in solid phase. This method can reduce the fluctuation of source term in solid phase conservative equations. It has been justified by the fact that prediction of the major elements of coal is not affected by ignoring limestone.[36–39] However, in the one-step hydrogen production gasifier, the composition of gases is significantly influenced by the multi-spices in solid phase. It is necessary to include the other species of solid phase in gasification model.

In this study, the coal gasification model was developed from Single-species of Solid Phase (SSP) method to Multi-species of Solid Phase (MSP) method. The second species of solid phase is CaO. It is applied not only to fix H_2S but to absorb CO_2. By right of the water gas shift reaction, higher concentration of H_2 is produced due to the conversion of CO and the absorption of CO_2. With the process going on, more new species are created in the solid phase, such as $Ca(OH)_2$, $CaCO_3$, and CaS. Therefore, it is important to adopt MSP method to describe the complicated process of hydrogen production in coal gasifier. Compared with SSP method, more transport equations in solid phase are used besides different

heterogeneous reactions in MSP method. The presented model unifies the two aspect of the one-step hydrogen production, that is, flow field and gasification reaction. The variable density and thermal conductivity are taken into account to approximate the process of mass transfer and heat transfer in solid phase. Predicted results are compared with the measurements of flow field[40] and gas products concentration[41,42] in laboratory-scale plants.

Model

A sketch of the entrained flow gasifier is shown in Figure 1. The inner diameter of Hastelloy tube is 0.02 m, and the height of the riser is 1.8 m. This gasifier is built as high pressure flow type.[41] While Coal/CaO mixture and high pressure steam are continuously injected from the bottom, the gas and solid reaction products are continuously removed from the top. The operating pressure is from 0.1 to 6 MPa. After the system pressure stabilizes, the coal/CaO mixture is injected at a rate of 1.67×10^{-5} kg/s to start the reactions. The superficial gas velocity is operated at the range of 0.053–3.49 m/s. The reactor temperature is maintained at 923 K. In this gasifier, hydrogen in high yield is produced with little release of CO_2 by gasification of coal with steam in the presence of CaO as CO_2 sorbents. CaO is not only as accepter of CO_2 and other pollutants such as H_2S, but also as catalyst to achieve reforming, gas water shift reaction and coal gasification simultaneously in a single reactor.[43,44] Ohtsuka et al.[45] found that the addition of calcium catalyst can also decrease the reaction temperature and increase the gasification rate.

Coal gasification reactions

At the entrance, Char and CaO which belong to solid phase are injected. Later in the reactor, more species in solid phase are created such as $Ca(OH)_2$, $CaCO_3$ and CaS. In this work, these species are assumed to share the same solid velocity, but have their own transport equation. Consulting with Lin et al.[46] and Mondal et al.s'[4] suggestion, more detailed reaction scheme for hydrogen production is described in the gasifier models. There are five processes in this reaction scheme, namely pyrolysis, tar cracking, char gasification, CO_2, and H_2S fixation, and gas phase reactions.

Pyrolysis At the feed position, the drying process and the devolatilization reactions take place very quickly according to experimental results,[38] so it is assumed that the pyrolytic process of the raw coal is completed in this region. The yield of each product is determined by the proximate analysis of the raw coal. The sum of the mass fraction of products is calculated to be unity in the raw coal.

$$Y_{\mathrm{Char}} + Y_{\mathrm{Volatile}} + Y_{\mathrm{Water}} + Y_{\mathrm{ash}} = 1$$

$$\mathrm{Coal} \rightarrow \mathrm{Char(s)} + \mathrm{Volatile(g)} + \mathrm{H_2O(g)} + \mathrm{Ash(s)} \qquad \text{(R1)}$$

The following chemical process is pyrolysis of the released volatile. There is no standard chemical stoichiometrically equation for the pyrolysis of the volatile due to its complex composition. For the sake of simplification, it was assumed that the molecular formula of the volatile is determined by the final pyrolysates.[33–35] In the present work, the composition of volatile matter can be deduced from pyrolysis results

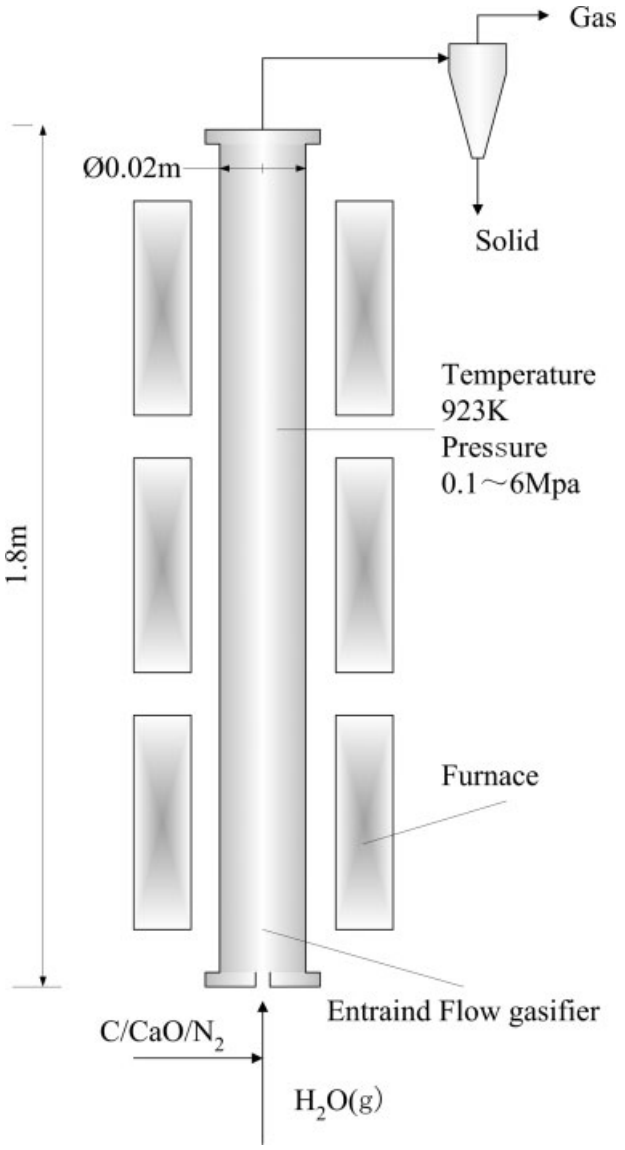

Figure 1. Configuration of the entrained flow gasifier (Lin, Harada et al. 2004).

of experiments for hydrogen production.[3,41] Kinetic constants for primary pyrolysis and tar cracking were derived from Brown et al.[12]

$$\mathrm{Volatile} \rightarrow v_1\mathrm{CO_2} + v_2\mathrm{CO} + v_3\mathrm{H_2} + v_4\mathrm{CH_4} + v_5\mathrm{C_2H_6} + v_6\mathrm{C_2H_4} + v_7\mathrm{H_2S} + v_8\mathrm{NH_3} + v_9\ \mathrm{tar} \qquad \text{(R2)}$$

$$R_2 = v_i K_2 [\mathrm{Volatile}]^{0.2} \qquad (1)$$

Taiheiyo coal was used as experimental material, whose properties are listed in Table 1. Combined the proximate analysis with the ultimate analysis, the molecular formula of the volatile can be determined as $C_{35}H_{70.91}O_{7.41}N_{1.02}S_{0.11}$. The composition of tar is usually regarded as condensed-nuclei aromatics, and Wang[47] calculated its molecular weight as 325 from the experimentation of coal pyrolysis. Thus, the

Table 1. Material Analyses and Properties

Parameters	Values
Proximate analysis (wt %)	
Moisture	4.8
Volatile matter	48.8
Fixed carbon	38.8
Ash	7.6
Ultimate analysis (wt %)	
Carbon	77.4
Hydrogen	6.6
Nitrogen	1.2
Oxygen	14.6
Sulfur	0.3
Others	
Mean particle size (mm)	0.045
Coal Density (kg/m^3)	1220
CaO Density (kg/m^3)	3320
Coal/CaO ratio (wt/wt)	1/2

molecular formula of the tar can be reckoned as $C_{21.4}H_{27.7}O_{2.2}N_{0.27}S_{0.1}$.

Tar Cracking. The secondary pyrolysis will occur while the tar is still in the reactor. As reported by Lin et al.,[48] $CaO/CaCO_3$ can facilitate tar cracking, leading to H_2, CH_4, and coke formation. They thought that $CaO/CaCO_3$ catalysis primarily affects tar decomposition outside the char, rather than the coal pyrolysis occurring inside the particles, because the $CaO/CaCO_3$ solid is only physically mixed, added to the outsides of the coal particles.

$$\text{tar} \rightarrow v_{10}H_2 + v_{11}CH_4 v_{12}\text{Char(s)} \tag{R3}$$

$$R_3 = v_i K_3 [\text{Tar}]^{0.2}(1 + Y_{CaO} + Y_{CaCO_3}) \tag{2}$$

Heterogeneous Reactions. Gas-solid reactions are including the processes of char gasification and gas pollutants (CO_2, H_2S) fixation. The different reaction mechanisms are taken into account. Combining diffusion effect with kinetic model is the main solution to handle heterogeneous reactions. For example, the unreacted core model with diffusion resistance was used in the literatures of Souza-Santos and Chejne.[49,38] In Eaton and Smoot's review,[50] char oxidation model based on measured intrinsic char kinetic rates and a pore diffusion model was presented by Reade et al.[50] To account for the simultaneous effects of the different resistances (diffusion through the gas film, surrounding the particle, and intrinsic chemical kinetics), Di Blasi[33] assumed a linear dependency on the oxidizing/gasifying species concentration to propose char gasification models.

In this study, char and CaO particles were assumed as spherical particles surrounded by a stagnant boundary layer through which gas species must diffuse before they react with the char or CaO. The overall reaction rate of a particle is determined by the diffusion of gases and the kinetic reactions.

The char gasification reactions are as following and their kinetic constants are derived from Neogi et al.[36]

$$C + H_2O \rightarrow CO + H_2 \tag{R4}$$

$$C + CO_2 \rightarrow 2CO \tag{R5}$$

$$C + H_2 \rightarrow CH_4 \tag{R6}$$

The gas pollutants (CO_2 and H_2S) fixations are

$$CaO + H_2O \rightarrow Ca(OH)_2 \tag{R7}$$

$$CaO + CO_2 \rightarrow CaCO_3 \tag{R8}$$

$$Ca(OH)_2 + CO_2 \rightarrow CaCO_3 + H_2O \tag{R9}$$

$$CaO + H_2S \rightarrow CaS + H_2O \tag{R10}$$

The units of the corresponding kinetic constants should be changed as same as that of the char gasification.

$$K_{Ar} = K_i d_s \tag{3}$$

where, K_{Ar} is kinetic rate constant, K_i are kinetic rate constants of R7–R10 in the references, and d_s is the average particle diameter of Char and CaO.

The diffusion rate constants can be derived from the definition of Sherwood number

$$K_{Dif} = \frac{ShD_{gs}w_{sj}}{RT_s d_s} \tag{4}$$

where, K_{Dif}, Sh, D_{gs}, $w_{s,j}$, R and T_s are diffusion rate constant, Sherwood number, Mass diffusion coefficient, molecular weight of solid phase, the universal gas constant and temperature of solid phase, respectively. Breault[51] provided a critical review to guide the selection of the best Sherwood number correlation in circulating fluidized bed reactors. In this study, the effect of phase volume fraction is neglected to avoid computational difficulty. The Sherwood number is written as

$$Sh = 2.0 + 0.552Re^{1/2}Pr^{1/3} \tag{5}$$

where, Re and Pr are Reynolds number and Prandtl number, respectively.

The heterogeneous reaction rate is obtained as a mixture of kinetic and diffusion controlled mass transfer rate, which came from unreacted-core model.[35,51]

$$R_{s,g} = \eta_j \frac{6r_s}{d_s}\left[(K_{Dif})^{-1} + (K_{Ar})^{-1}\right]^{-1} C_{g,i} \tag{6}$$

This model only deals with one solid species such as Char in Colomba's work.[33] In this work, many solid species such as CaO, $Ca(OH)_2$, $CaCO_3$ and CaS are included. It is assumed that these solid species compose the whole solid phase and they share solid volume fraction and particle diameter. The heterogeneous reaction rate of each solid species is given by multiplying its molar fraction.

$$R_{s,g} = \eta_j \frac{6r_s}{d_s}\left[(K_{Dif})^{-1} + (K_{Ar})^{-1}\right]^{-1} C_{g,i}\left(\frac{Y_{s,j}/W_{s,j}}{\sum_{j=1}^{N} Y_{s,j}/W_{s,j}}\right) \tag{6.1}$$

where, η_j, r, C and Y are the effectiveness factor, volume fraction, concentration and mass fraction, respectively. In

addition, the decomposition temperature of $Ca(OH)_2$ is 853 K. For R7, it should be limited at this temperature, this is, if the temperature of $Ca(OH)_2$ is higher than 853 K, reaction rate is zero.

Homogeneous Reactions. After pyrolysis of volatile, tar cracking and char gasification, the reactive gas species are produced. These gas species can be continuing to react with each other. The main reactions can be summarized as water-gas shift and methane steam reforming, which are reversible reactions. For in situ CO_2 removal utilizing the CaO carbonation, it is of great advantage to change these processes in the direction of hydrogen production. Lee et al.[52] carried out a mathematical model and reaction experiment to describe the processes of the CaO carbonation enhanced reforming and shift reactions. The intrinsic rate equations of Lee's model came from Xu and Froment's literature.[53] Many improvements have been developed to be good match in other reaction conditions.[54–56] Here, calcium catalyst was applied into the reforming and shift reaction system, instead of a Ni/$MgAl_2O_4$ catalyst. Its catalytic activity is lower than that of Ni/$MgAl_2O_4$ catalyst. Thus, the modified intrinsic equations should be calculated to describe the reforming and shift reaction at low rate.

$$CH_4 + H_2O \leftrightarrow CO + 3H_2 \tag{R11}$$

$$CO + H_2O \leftrightarrow CO_2 + H_2 \tag{R12}$$

$$CH_4 + 2H_2O \leftrightarrow CO_24H_2 \tag{R13}$$

$$R_{11} = \frac{\eta_{11} r_g \rho_{CaO} \frac{K_{11}}{p_{H_2}^{2.5}} \left(p_{CH_4} p_{H_2O} - \frac{p_{H_2}^3 p_{CO}}{K_{11}^*} \right)}{(DEN)^2} \tag{7}$$

$$R_{12} = \frac{\eta_{12} r_g \rho_{CaO} \frac{K_{12}}{p_{H_2}} \left(p_{CO} p_{H_2O} - \frac{p_{H_2} p_{CO_2}}{K_{12}^*} \right)}{(DEN)^2} \tag{8}$$

$$R_{13} = \frac{\eta_{13} r_g \rho_{CaO} \frac{K_{13}}{p_{H_2}^{3.5}} \left(p_{CH_4} p_{H_2O}^2 - \frac{p_{H_2}^4 p_{CO_2}}{K_{13}^*} \right)}{(DEN)^2} \tag{9}$$

$$DEN = 1 + K_{CO} p_{CO} + K_{H_2} p_{H_2} + K_{CH_4} p_{CH_4} + \frac{K_{H_2O} p_{H_2O}}{p_{H_2}} \tag{10}$$

where, $p_i (i = CH_4, H_2O, H_2, CO, CO_2)$ is the partial pressure of species i. $K_i (i = CO, H_2, CH_4, H_2O)$ is adsorption constant. K_{11}, K_{12}, K_{13} are rate coefficient of reaction. K^* is the equilibrium constant. ρ is the density.

The Arrhenius coefficients related to the R2–R13 are listed in Table 2.

Gas-Solid Governing Equations. The KTGF developed by Neri[24] and Tartan[40] was applied to simulate flow of FCC particles in the IIT riser. The fully developed core annular structure can be observed in the simulation of their works. In this study, their models are further developed to consider the effect of heat transfer and chemical reaction. Source terms have been added to the instantaneous governing equations of mass and momentum. This is because gas-solid reactions lead to interphase transfer.

The continuity equations for gas and solid phases are given by

$$\frac{\partial}{\partial t}(r_g \rho_g) + \nabla \cdot (r_g \rho_g u_g) = S_{s,g} \tag{11}$$

$$\frac{\partial}{\partial t}(r_s \rho_s) + \nabla \cdot (r_g \rho_s u_s) = S_{g,s} \tag{12}$$

where, r, ρ and u are the volume fraction, the density ,and the velocity, respectively. S on the right hand is the source term and set to zero only in flow field such as Neri and Tartan's work.[24,40] When the governing equations are used in heterogeneous reaction, there are mass, momentum, and heat transfer between gas phase and solid phase. In the present work, coal reacting with steam, hydrogen and carbon dioxide changes solid phase into gas phase. Steam and carbon dioxide reacting with calcium oxide change gas phase into solid phase. Thus, mass source for the phases yield

$$S_{s,g} = R_{s,g}\left(\sum \gamma_i^p w_i^p - \sum \gamma_i^r w_i^r \right) = S_{g,s} \tag{13}$$

For the gas phase density, a mixture of ideal gas was assumed

$$\rho_g = \frac{p}{RT \sum_{i=1}^{n} \frac{Y_i}{w_i}} \tag{14}$$

where, p, T, Y_i and w_i are gas pressure, gas mixture mean temperature, mass fraction and the molecular weight for every species respectively.

The solid phase density is defined as the mixture density for each species in solid phase

$$\rho_s = \frac{1}{\sum_{j=1}^{n} \frac{Y_j}{\rho_j}} \tag{15}$$

The momentum equation for gas and solid phase can be written as

$$\frac{\partial}{\partial t}\left(r_g \rho_g u_g\right) + \nabla \cdot \left(r_g \rho_g u_g u_g\right) = - r_g \nabla P - \Phi_{gs}\left(u_g - u_s\right) + \left(\nabla \cdot r_g \tau_g\right) + r_g \rho_g g + S_{Ms,g} \tag{16}$$

$$\frac{\partial}{\partial t}(r_s \rho_s u_s) + \nabla \cdot (r_s \rho_s u_s u_s) = - r_s \nabla P - p_s\, \Phi_{gs}\left(u_s - u_g\right) + (\nabla \cdot r_s \tau_s) + r_s \rho_s g + S_{Mg,s} \tag{17}$$

On the righthand side of Eqs. 6 and 7, the terms $S_{Mg,s}$ and $S_{Ms,g}$ describe interphase momentum transfer. They can be assumed that the reactants mix (conserving momentum) and the products take momentum in the ratio of the rate of their formation.

$$S_{Ms,g} = R_{s,g}\left(\sum \gamma_i^p w_i^p u_{net} - \sum \gamma_i^r w_i^r u_i \right) = -S_{Mg,s} \tag{18}$$

The net velocity u_{net} is written as

$$u_{net} = \frac{\sum \gamma_i^r w_i^r u_i^r}{\sum \gamma_i^r w_i^r} \tag{19}$$

In addition, Φ_{gs} is the drag coefficient between the gas phase and solid phase, and g is gravity.

Table 2. Arrhenius Coefficients Related to the R2–R13

Reaction	Kinetic	Reference
R2	$K_2 = 3.7 \times 10^5 \exp[-25018/T_g]/s$	Brown et al.[12]
R3	$K_3 = 1.46 \times 10^5 \exp[-40052/T_g]/s$	Brown et al.[12]
R4	$K_4 = 8.33 \times 10^{-2} \exp[-14603.92/T_s]m/s$	Neogi et al.[36]
R5	$K_5 = 5.56 \times 10^3 \exp[-43308.28/T_s]m/s$	Neogi et al.[36]
R6	$K_6 = 0.208 \exp[-27697/T_s]m/s$	Neogi et al.[36]
R7	$K_7 = 1.78 \times 10^3 \exp[-5256.19/T_s]/s$	Chen et al.[61]
R8	$K_8 = 1.72 \times 10^2 \exp[-8684.15/T_s]/s$	Lee et al.[52]
R9	$K_9 = 1.72 \times 10^5 \exp[-8684.15/T_s]/s$	Estimated as in Lee et al.[52]
R10	$K_{10} = 1.50 \times 10^4 \exp[-25542/T_s]/s$	Zhong et al.[68]
R11	$K_{11} = 1.174\times10^{12} \exp[-28879/T_g]kmol/(kg\ cat\ pa\ s)$	Xu and Froment[53]
	$K^*_{11} = 4.71 \times 10^{12} \exp[-26942.51/T_g]pa^2$	Xu and Froment[53]
R12	$K_{12} = 543.06 \exp[-8074.3/T_g]kmol/(kg\ cat\ Pa\ s)$	Xu and Froment[53]
	$K^*_{11} = 1.142 \times 10^{-2} \exp[-4486.41/T_g]$	Xu and Froment[53]
R13	$K_{13} = 2.83 \times 10^{11} \exp[-29336/T_g]kmol/(kg\ cat\ Pa\ s)$	Xu and Froment[53]
	$K^*_{13} = K^*_{11} \times K^*_{12} Pa^2$	Xu and Froment[53]
	$K_{CH_4} = 0.179 \exp\left[\frac{38320}{R}\left(\frac{1}{T}-\frac{1}{823}\right)\right]Pa^{-1}$	Xu and Froment[53]
	$K_{H_2O} = 0.4152 \exp\left[-\frac{88680}{R}\left(\frac{1}{T}-\frac{1}{823}\right)\right]$	Xu and Froment[53]
	$K_{CO} = 40.91 \exp\left[\frac{70650}{R}\left(\frac{1}{T}-\frac{1}{648}\right)\right]Pa^{-1}$	Xu and Froment[53]
	$K_{H_2} = 0.0296 \exp\left[\frac{82900}{R}\left(\frac{1}{T}-\frac{1}{648}\right)\right]Pa^{-1}$	Xu and Froment[53]

The gas-solid drag was specified for different solid concentration.[24] If $r_g < 0.8$, the well-known Ergun equation is suitable for describing the dense regime.

$$\Phi_{gs} = 150\frac{(1-r_g)r_s\mu_g}{r_g d_s^2} + 1.75\frac{\rho_g r_s|u_g - u_s|}{d_s} \tag{20}$$

If $r_g \geq 0.8$, the drag coefficient was given based on the work by Wen and Yu

$$\Phi_{gs} = \frac{3}{4}C_d\frac{|u_g - u_s|}{d_s}r_g^{-2.65} \tag{21}$$

where,

$$C_d = \begin{cases} \frac{24}{Re}(1+0.15Re^{0.687}) & Re \leq 1000 \\ 0.44 & Re > 1000 \end{cases} \tag{22}$$

$$Re = \frac{|u_g - u_s|r_g\rho_g d_s}{\mu_g} \tag{23}$$

The stress tensor τ_g is given by

$$\tau_g = \mu_g(\nabla u_g + \nabla u_g^T) - \frac{2}{3}\mu_g \nabla . u_g \tag{24}$$

And the solid stress tensor τ_s is given by

$$\tau_s = \left(\lambda_s - \frac{2}{3}\mu_s\right)\nabla u_s + \mu_s(\nabla u_s + \nabla u_s^T) \tag{25}$$

In the equation above, λ_s is bulk viscosity, which can be obtained as follow

$$\lambda_s = \frac{4}{3}r_s\rho_s d_s g_0(1-e)\left(\frac{\Theta_s}{\pi}\right)^{1/2} \tag{26}$$

And the equation of the solid shear viscosity μ_s is

$$\mu_s = \frac{4}{5}r_s^2\rho_s d_s g_0(1+e)\sqrt{\frac{\Theta_s}{\pi}} + \frac{10\rho_s d_s\sqrt{\pi\Theta_s}}{96(1+e)\varepsilon_s g_0}\left[1+\frac{4}{5}g_0 r_s(1+e)\right]^2 \tag{27}$$

The solid pressure p_s is defined in analogy with μ_s and consists of a collision and a kinetic term

$$p_s = r_s\rho_s\Theta_s + 2(1+e)r_s^2 g_0\rho_s\Theta_s \tag{28}$$

where, Θ_s is granular temperature; e is the coefficient of restitution for particle collisions; g_0 is the radial distribution function.

For the radial distribution function of solid phase, g_0 is expressed as

$$g_0 = \left[-\left(\frac{r_s}{r_{s,max}}\right)^{1/3}\right]^{-1} \tag{29}$$

The granular temperature Θ_s is a pseudo-temperature which can be defined as

$$\frac{3}{2}\Theta_s = \frac{1}{2}\langle u_s' u_s'\rangle \tag{30}$$

where, u_s' is the fluctuating velocity of the particles and can be derived from

$$u_s' = U_s - u_s \tag{31}$$

where, U_s is the instantaneous velocity of the particles. The solid mean velocity u_s is defined as

$$u_s = \langle U_{s,i}\rangle = \frac{1}{n}\int U_{s,i} f \mathrm{d}U_s \tag{32}$$

where, f, n are single-particle velocity distribution function and particle number density respectively.

The details can be found from Ding and Gidaspow's work,[59] where the derivation of the granular temperature transport equation has been reported.

Granular temperature transport equation for the solid[59]

$$\frac{3}{2}\left[\frac{\partial}{\partial t}(r_s\rho_s\Theta_s) + \nabla\cdot(r_s\rho_s\Theta_s u_s)\right] = -(p_s\bar{\bar{I}} + \bar{\bar{\tau}}_s):\nabla\vec{u}_s + \nabla\cdot(k_s\nabla\Theta_s) - \gamma - 3\Theta_{gs}\Theta_s \tag{33}$$

The diffusion coefficient for granular energy k_s is given by

$$k_s = \frac{150\rho_s d_s\sqrt{\Theta_s\pi}}{384(1+e)g_0}\left[1+\frac{6}{5}r_s g_0(1+e)\right]^2 + 2\rho_s r_s^2 d_s g_0(1+e)\sqrt{\frac{\Theta_s}{\pi}} \tag{34}$$

The dissipation of fluctuating energy due to inelastic collision takes the form

$$\gamma = 3(1-e^2)r_s^2\rho_s d_s g_0\Theta_s\left[\frac{4}{d_s}\left(\sqrt{\frac{\Theta_s}{\pi}}\right) - \nabla u_s\right] \tag{35}$$

Gas phase is assumed as a mixture of 12 species, represented by their mass fraction as follows: Volatile, CO_2, H_2O, CO, H_2, CH_4, C_2H_4, C_2H_6, H_2S, NH_3, Tar, and N_2. Solid phase includes six species, this is, Char, CaO, $CaCO_3$, $Ca(OH)_2$, CaS, and Ash. The conservation equations for these chemical species can be represented but the N_2 for gas phase and Ash for solid phase, which are computed from the fact that the sum of all mass fractions is equal to one in the gas phase and solid phase, respectively.

$$\frac{\partial}{\partial t}(\rho_g r_g Y_{g,i}) + \nabla(\rho_g r_g u_g Y_{g,i}) = -\nabla\cdot r_g J_{g,i} + r_g w_{g,i} R_{g,i} + S_{s,g} \tag{36}$$

$$\frac{\partial}{\partial t}(\rho_s r_s Y_{s,i}) + \nabla(\rho_s r_s u_s Y_{s,i}) = -\nabla\cdot r_s J_{s,i} + r_s w_{s,i} R_{s,i} + S_{g,s} \tag{37}$$

where, $J_{g,i}$ and $J_{s,i}$ are the diffusion flux of species i in gas phase and solid phase, respectively. $R_{g,i}$ and $R_{s,i}$ are the net rate of production of homogeneous species i and $S_{s,g}$ and $S_{g,s}$ are the heterogeneous reaction rate.

$$S_{s,g} = R_{s,g}\left(\sum\gamma_i^p w_i^p - \sum\gamma_i^r w_i^r\right) = -S_{g,s} \tag{38}$$

In the species transport equations of gas phase and solid phase, mass diffusion coefficients are used to calculate the diffusion flux of chemical species using the Fick's law

$$J_{g,i} = -\rho_g D_{g,i}\nabla\cdot Y_{g,i} \tag{39}$$

$$J_{s,i} = -\rho_s D_{s,i}\nabla\cdot Y_{s,i} \tag{40}$$

where the diffusion coefficient of the mixture for gas, $D_{g,i}$ is calculated from the binary mass diffusion coefficient $D_{i,j}$ as follow

$$D_{g,i} = \frac{1-X_i}{\sum_{j\neq i}\frac{X_j}{D_{i,j}}} \tag{41}$$

And the diffusion coefficient of the mixture for solid, $D_{s,i}$ is assumed as constant 2.88×10^{-5}, which is like gas due to the fact that particle fluidization has fluid properties. The value of $D_{s,i}$ is also in the range of Yang's data.[60]

The energy transport equations are solved for the specific enthalpy of gas phase and solid phase, which take the form:

$$\frac{\partial}{\partial t}(r_g\rho_g H_g) + \nabla\cdot(r_g\rho_g u_g H_g) = \nabla(r_g\alpha_g\nabla T_g) + Q_{s,g} + S_{Hs,g} \tag{42}$$

$$\frac{\partial}{\partial t}(r_s\rho_s H_s) + \nabla\cdot(r_s\rho_s u_s H_s) = \nabla(r_s\alpha_s\nabla T_s) + Q_{g,s} + S_{Hg,s} \tag{43}$$

where, H, α, Q are the specific enthalpy, the mixture thermal conductivity and the intensity of heat exchange between the gas and solid phases, respectively. The source terms for gas and solid are the heat transfer due to heterogeneous reactions leading to transformation from one phase to another.

$$S_{Hs,g} = R_{s,g}\left(\sum\gamma_i^p w_i^p H_{net} - \sum\gamma_i^r w_i^r H_i\right) = -S_{Hg,s} \tag{44}$$

The net enthalpy of the reactants H_{net} is given by

$$H_{\text{net}} = \frac{\sum \gamma_i^r w_i^r H_i^r}{\sum \gamma_i^r w_i^r} \tag{45}$$

The specific enthalpy is defined by

$$H = \sum_{i=1}^{n} Y_i H_i \tag{46}$$

where, H_i is the enthalpy for each chemical species in the mixture and considers both thermal and chemical enthalpy:

$$H_i = \int_{T_0}^{T} C_{\text{p},i} dT + \Delta H_{\text{f},i} \tag{47}$$

where, the term T_0, $C_{\text{p},i}$ and $\triangle H_{\text{f},i}$ are the reference temperature, the heat capacity at constant pressure for the ith species, and the enthalpy of formation for the ith species in the standard state.

For the ideal gas, the mixture thermal conductivity is computed as

$$\alpha_{\text{g}} = \sum_{i=1}^{n} \frac{X_i \alpha_i}{\sum_{i \neq j} X_j \phi_{ij}} \tag{48}$$

where, $\phi_{ij} = \dfrac{\left[1+\left(\frac{\mu_i}{\mu_j}\right)^{1/2}\left(\frac{w_j}{w_i}\right)^{1/4}\right]}{\left[8\left(1+\frac{w_i}{w_j}\right)\right]^{1/2}}$, and X_i is the molar fraction of the ith species.

Thermal conductivity of the solid is given by

$$\alpha_{\text{s}} = \sum_{j=1}^{n} Y_j \alpha_j \tag{49}$$

The heat exchange between phases can be expressed as a function of the temperature difference and conform to the local balance condition $Q_{\text{gs}} = -Q_{\text{sg}}$.

$$Q_{\text{gs}} = h_{\text{gs}}\left(T_{\text{g}} - T_{\text{s}}\right) \tag{50}$$

where, h_{gs} is the heat transfer coefficient between the gas phase and the solid phase, and expressed in terms of a nodimensional Nusselt number

$$h_{\text{gs}} = \frac{Nu \cdot \alpha_{\text{g}} \cdot A_{\text{s}}}{d_{\text{s}}} = \frac{6 r_{\text{s}} \cdot Nu \cdot \alpha_{\text{g}}}{d_{\text{s}}^2} \tag{51}$$

The Nusselt number was proposed as the following empirical correlation by Gunn.[61]

$$Nu = (7 - 10 r_{\text{g}} + 5 r_{\text{g}}^2)\left(1 + 0.7 Re^{0.2} pr^{1/3}\right) + \left(1.33 - 2.4 r_{\text{g}} + 1.2 r_{\text{g}}^2\right)\left(Re^{0.7} Pr^{1/3}\right) \tag{52}$$

where, the continuous phase Prandtl number is defined by

$$Pr = \frac{\mu_{\text{g}} C_{\text{p,g}}}{\alpha_{\text{g}}} \tag{53}$$

Numerical considerations

A kinetic theory-based TFM was validated by the experimental data and simulation results reported by Neri[24] and Tartan.[40] The IIT risers in their experimentation and simulation are fed at the nozzle on the bottom part of the reactor. Tartan replaced Neri's U-type outlet with a splash plate to avoid the nonsymmetrical behavior. In this study, Tartan's riser was numerically simulated to get a comparison with experimental data. Using the same method, the simulation of Lin's gasifier was also carried out. In Lin's gasifier, the outflow of entrained flow gasifier is in vertical upward, and the symmetrical structure of the flow field can be observed. Two-dimensional axisymmetric form of governing equations has been applied for the description of the entrained flow gasifier. Figure 2 shows

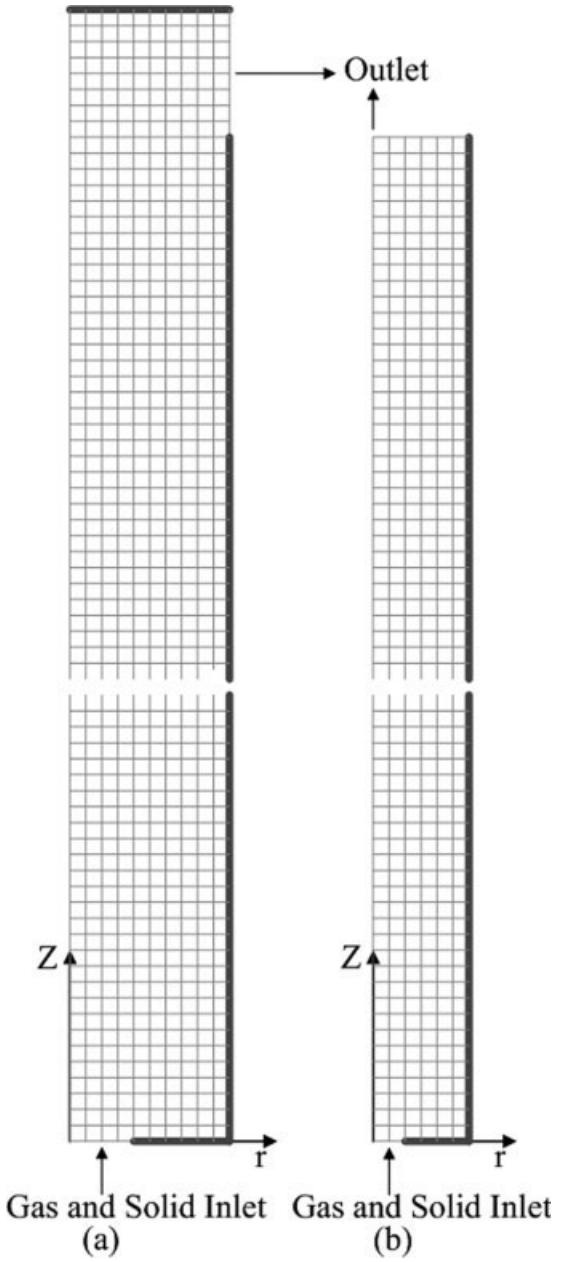

Figure 2. Tartan's riser geometry (a) and Lin's entrained flow gasifier geometry (b).

Table 3. Simulation Conditions and System Properties for Tartan's Riser

Riser diameter	7.62 cm
Riser inlet diameter	4.23 cm
Riser height	699 cm
Particle size	530 μm
Particle density	2.46 g/cm^3
Restitution coefficient (e)	0.98
Wall restitution coefficient (e_w)	0.6
Specularity coefficient	0.6
Solid mass flux	1.42 g/cm^2 s
Gas superficial velocity	490 cm/s
Grid size	0.423 $\times$ 1.50 cm^2
Grid number	11(radial) $\times$ 466(axial)
Time step	5×10^{-5}

the sketches of Tartan's riser geometry[40] and Lin's entrained flow gasifier[41] in the simulation. Table 3 gives the simulation conditions and system properties for Tartan's riser, which can be applied into Lin's entrained flow gasifier too. Table 4 shows the operating conditions and experimental results for Lin's entrained flow gasifier. The no-slip wall boundary condition is used for the gas phase while the solid phase is in Johnson and Jackson boundary condition, which is partial-slip.

$$u_{s,w} = -\frac{6\mu_s r_{s,max}}{\sqrt{3}\pi\varphi\rho_s r_s g_0\sqrt{\Theta}}\left.\frac{\partial u}{\partial n}\right|_{wall} \tag{54}$$

$$\Theta_w = \left(\frac{\kappa_s\Theta}{\gamma_w}\right)\left.\frac{\partial\Theta}{\partial n}\right|_{wall} + \frac{\sqrt{3}\pi\varphi\rho_s r_s u_{s,w}^2 g_0\Theta_w^{3/2}}{6r_{s,max}\gamma_w} \tag{55}$$

$$\gamma_w\frac{\sqrt{3}\pi\left(1-e_w^2\right)r_s\rho_s g_0\Theta_w^{3/2}}{4r_{s,max}} \tag{56}$$

The entrained flow gasifier model has been calculated using FLUENT (v.6.2.16). The present submodels were added via a User C Language interface. In FLUENT, the Phase Coupled SIMPLE (PC-SIMPLE) algorithm is available to solve velocity-pressure coupled differential equations. It generally will yield more accurate results by choosing the second-order discretization. Here the QUICK scheme is used. When the governing equations are discretized into algebraic equations, it can be solved numerically. To decrease the impact of the strong nonlinear characteristic of the model and ensure the good convergence and acceptable computational time, the Selective Algebraic Multigrid (SAMG) solver is used to solve the multiphase granular flow equations. The details on QUICK scheme and SAMG can be obtained from FLUENT user's Guide. In these equations, a tight convergence tolerance on the pressure equation can be used to avoid volume imbalance errors in the volume fraction equations. The convergence criteria require that the scaled residuals decrease to 10^{-3} for continuity, momentum and granular temperature transport equations, while 10^{-6} for energy and species equations.

Results and Discussion

Flow field model comparison with experiments

The gas-solid flow model with kinetic theory was validated by the solid velocity, volume fraction, granular temperature, and solid viscosity. These experimental results were obtained in the IIT riser reported by Tartan et al.[40] In the experiments, Particle Image Velocimetry (PIV) was used to measure the axial, radial, and tangential velocities of the particles in the vertical pipes.

Figure 3 shows the radial distribution of the axial particle velocity at the height of 4.2 m. The experimental data were measured with a probe inserted from both side. Tartan et al.[40] presented flow model both in analytic and numerical solution to achieve the similar trend to the experimental data. Adopted this flow model, the calculated values are also obtained in good agreement with experimental values. The typical solid velocity profile is found in the computation, this is, the particle phase is in a core-annular type of flow.[25] Figure 4 is a comparison of calculated radial distribution of the particle concentration with experimental and simulated data of Tartan et al. It can be seen that the calculated value of solid volume fraction is slightly higher than that of the reported data. This is because the particle velocity has an adverse relationship with the solid fraction.

Figure 5 shows a comparison of the measured granular temperature to the numerical simulation. The granular temperature is proportional to the kinetic energy of the particles'

Table 4. Operating Conditions and Experimental Results for Lin's Entrained Flow Gasifier

No.	1	2	3	4	5
Total Pressure (MPa)	0.1	1.0	3.0	5.0	6.0
Coal/CaO mixture feed (10^{-3} kg/s)	0.0167	0.0167	0.0167	0.0167	0.0167
Water supply (10^{-3} kg/s)	0.153	0.151	0.145	0.133	0.128
N_2 supply [10^{-3} m^3(STP)/s]	0.13	0.13	0.13	0.13	0.13
Steam pressure (MPa)	0.06	0.6	1.7	2.8	3.2
Gas superficial velocity (m/s, 923 K)	3.49	0.35	0.12	0.064	0.053
Solid temperature at entrance (K)	300	300	300	300	300
Gas temperature at entrance (K)	868	868	868	868	868
Gas temperature of reactor (K)	923	923	923	923	923
Gas and solid temperature at exit (K)	803	803	803	803	803
Exp. result					
H_2 (%)	37	58	71	76	77
CH_4 (%)	27	23	21	17	16
C_2H_6 (%)	5	4	3	3	3
C_2H_4 (%)	4	3	2	2	2
CO (%)	15	7	1	0	0
CO_2 (%)	12	5	2	2	2

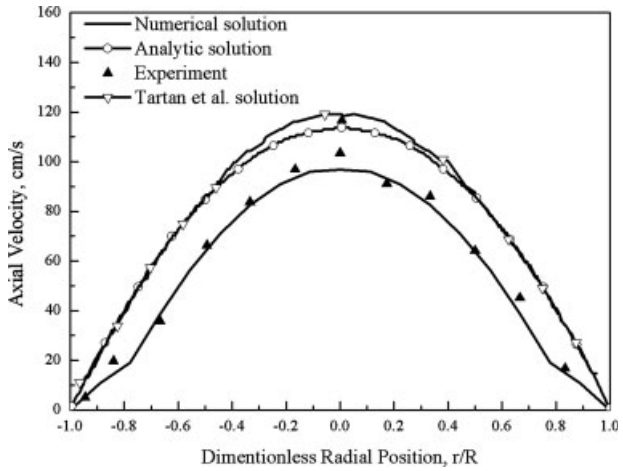

Figure 3. Calculated radial distribution of the axial particle velocity versus experimental and simulated data of Tartan et al. (Tartan and Gidaspow 2004).

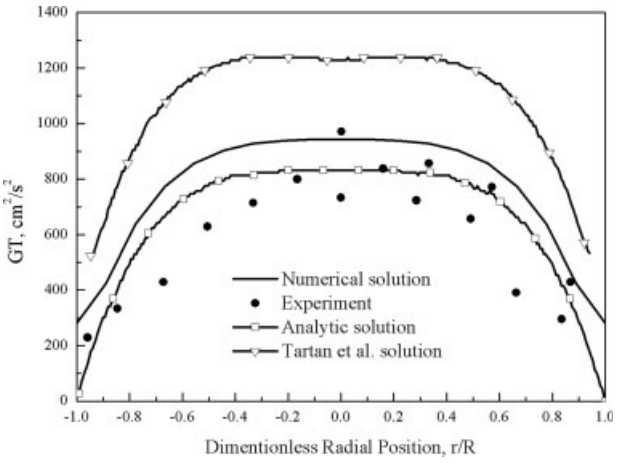

Figure 5. Calculated radial distribution of the granular temperature versus experimental and simulated data of Tartan et al. (Tartan and Gidaspow 2004).

random motion. It can be calculated from transport equation to predict the solid viscosity and the solid stress. Therefore, to obtain the precise prediction of particles motion, it is very important to validate the kinetic theory of gas-solid flow model by the measurement of granular temperature in the fluidized bed. The comparison between the computed and the experimental granular temperature is in reasonably good agreement. Moreover, the calculated value of solid viscosity compared with that of the experimentation and simulation of Tartan et al. is shown in Figure 6.

In view of the important influence of reaction pressure on enhancing coal conversion, maximizing H_2 output and CO_2 removal, the gas-solid flow characteristics is further validated at elevated operating pressures. The experimental data in this study were selected from the literature reported by Louge et al.[62] Table 5 lists the experimental conditions of Circulating Fluidized Bed (CFB) at the different operating pressures. The experimental CFBs are called Atmospheric Circulating Fluidized Bed (ACFB) and Pressurized Circulating Fluidized Bed (PCFB) respectively. Dimension analysis is employed to deal with the experimental data, so does the calculated data. As shown in Figure 7A, the elevation is shown as a fraction of riser height, $z^+ \equiv z/H$, and the static pressure relative to the riser top is made dimensionless as $p^+ \equiv (p - p_{top})/\rho_s gD$. The symbols in this figure represent the experimental points and the lines are the simulation resulting from the flow model. Comparisons between the static pressure profile of ACFB and PCFB suggest a smaller pressure gradient at the elevated operating pressure. A good agreement is observed between the flow model and the experimental work. It indicates that the flow model can be used to predict the gas-solid flow characteristics at elevated operating pressures.

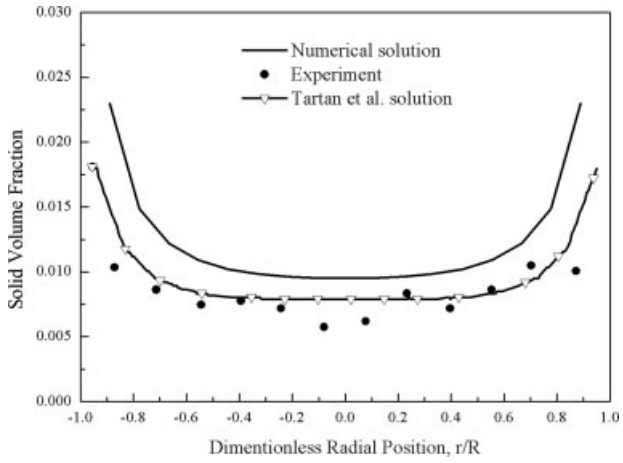

Figure 4. Calculated radial distribution of the particle concentration versus experimental and simulated data of Tartan et al. (Tartan and Gidaspow 2004).

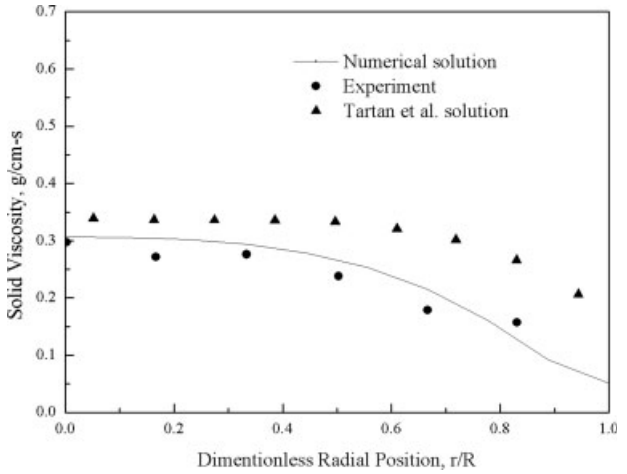

Figure 6. Calculated radial distribution of the solid viscosity versus experimental and simulated data of Tartan et al. (Tartan and Gidaspow 2004).

Table 5. Experimental Conditions

Type	ACFB	PCFB
Gas density (kg/m^3)	0.3	2.39
Gas viscosity [kg/(m s)]	1.94×10^{-5}	1.77×10^{-5}
Particle density (kg/m^3)	1440	1440
Equivalent diameter (m)	1.62×10^{-4}	1.5×10^{-4}
Operating parameters	Fr = 130	Fr = 130
	M/R = 0.0033	M/R = 0.0033
Pressure (atm)	1	8.15
Bed height (m)	7	7
Bed diameter (m)	0.2	0.2

Figure 7B shows a prediction of the static pressure changes along the bed height in Lin's entrained flow gasifier at the different operating pressures. It can be noted that the static pressure has a linear dependency on the bed height at the atmospheric condition. This is because the solid load is very dilute in the gasifier. While the operating pressure is varied from 0.1 to 6 MPa, the same trend of the static pressure changes with bed height can be observed as the Figure 7A.

Gasification model comparison with experiments

After Coal/CaO powder mixture had been fed into the Lin's entrained flow gasifier to react with steam at the temperature of 923 K and the different operating pressures, the concentrations of H_2, CH_4, C_2H_4, C_2H_6, CO, and CO_2 in the gas phase were continuously measured by micro-gas chromatography at the sampling port on the top of gasifier. The measured amount of gas composition increased with increasing reaction time at the initial stage. About 20 min later, gas concentrations were stable. When the operation was in steady, these gas samplings were calculated based on gas products except H_2O and N_2.[41] The gasification model is validated by these gas samplings with Taiheiyo coal at five different operating pressures. The simulated outlet molar fraction of gas composition can be compared with experimental data by the following form of area average.

$$\overline{X}_i = \frac{1}{A}\int X_i \mathrm{d}A \tag{57}$$

Figure 8 shows comparison of the model results with the experimental data in Lin's work. One-step hydrogen production is an incredibly complex chemical system. It is impossible to simulate this process in a general reaction mechanism. Only simplified reaction models can be used to describe the gasification process. Here, the Arrhenius coefficients of heterogeneous reactions came from atmospheric experiments[36,57,63] and the homogeneous reaction schemes were developed with the temperature range of 675–1000 K and the pressure range of 3–10 bar by Xu and Froment.[53] Although intrinsic rate equations might be included in their reaction models, prediction from extrapolation still has little accuracy if the reaction models are not further corrected in the practical experimental conditions. Therefore, adjustments were made on the kinetic parameters to fit the simulated results to the experimental observations by Neogi et al.[36] Effectiveness factors were adjusted to simulate steam reforming reactions and water-gas shift reaction reported by de Groot and Froment.[64] In this study, adjusted frequency factors and effectiveness factors are used to improve the simulated results. The adjusted frequency factors for the heterogeneous reactions listed in Table 2 should keep the reaction models fit roughly the closeness of the experimental results. The effectiveness factor accounts for the pore resistance in the pellet. Due to complicated pellet structure at the different operating pressures in Lin's gasifier, the values of effectiveness factors have to be estimated. These can compensate the discrepancy between the model and experimental data. The estimated effectiveness factors η are not only taken into account the diffusion resistance, but the Char and CaO reactivity and other external factors. The values of η listed in Table 6 vary over a range of 0–1. As shown in Table 6, the estimated effectiveness factor of Char is assigned a smaller value at the elevated pressures. On the contrary, the effectiveness factors used in the gas pollutants (CO_2 and H_2S) fixations and the homogeneous reactions are given larger values at the elevated pressures. This is because the reaction rate equations were obtained from the different experimental conditions. The Char gasification rates derived

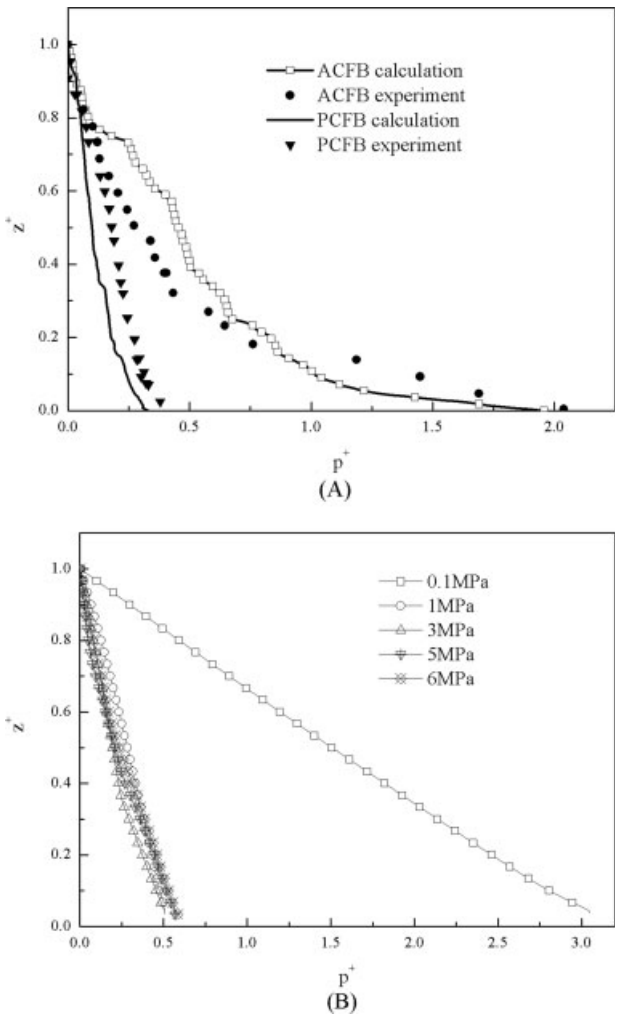

Figure 7. Static pressure profile along the bed height in dimensionless at different operating pressures(A) prediction and experiment (B) prediction of Lin's gasifier.

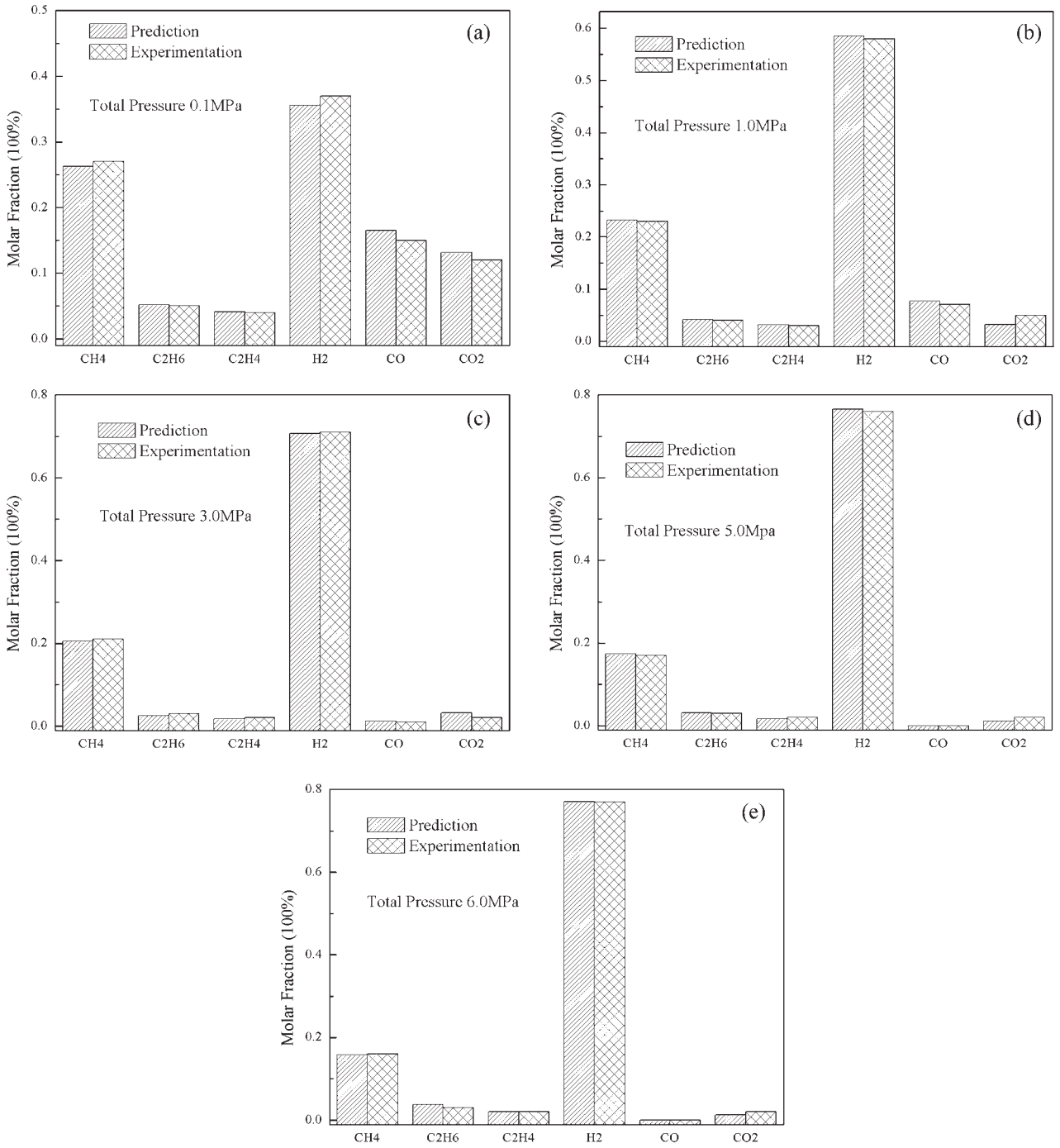

Figure 8. Comparisons of predictions and experimental data at different operating pressures.

Table 6. Estimated Effectiveness Factors

Case	η_{Char}	$\eta_{CaO/Ca(OH)2}$	η_{11}	η_{12}	η_{13}
0.1 MPa	0.8	0.1	0.02	0.02	0.01
1 MPa	0.5	0.2	0.03	0.08	0.02
3 MPa	0.2	0.7	0.07	0.7	0.06
5 MPa	0.2	0.7	0.07	0.7	0.06
6 MPa	0.2	0.7	0.07	0.7	0.06

from atmospheric experiments are significantly affected by gas reactant concentration in the gasification model. The calculated values would be much higher than experimental data at the elevated pressures if they were not corrected. Therefore, a smaller value of the estimated effectiveness factor is set at the higher operating pressure. However, more CO_2 should be fixed at the higher operating pressure. To avoid smaller calculated results, the larger effectiveness factors are

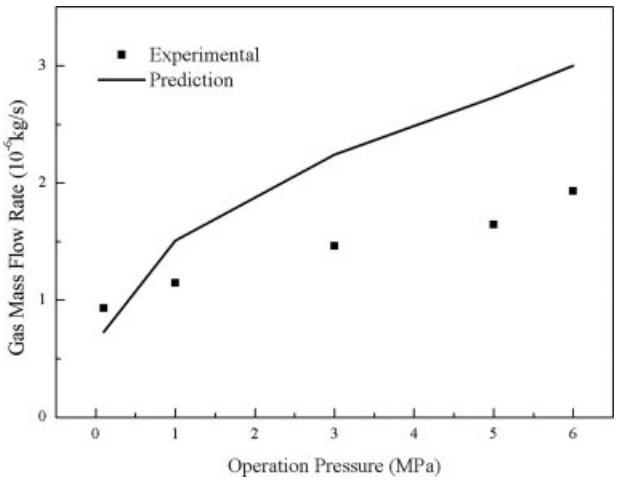

Figure 9. Effect of operating pressure on total gas mass flow rate.

set in the gas pollutants (CO_2 and H_2S) fixations at the higher operating pressure. The high concentration of Hydrogen mainly depends on synergistic effects of water-gas shift reaction and CO_2 absorption at the elevated pressure. This is because water-gas shift reaction is not pressure dependent and methane steam reforming reactions is favored by low pressure.[4] Therefore, the corresponding effectiveness factors are set in the homogeneous reactions according to the contribution for Hydrogen production. The values of the effectiveness factors at the operating pressure of 3–6 MPa are derived from the literature.[64] As shown in Figure 8, the exceptionally good agreements are observed at elevated pressures. This is because the homogeneous reaction schemes (R11–R13) were obtained at these pressure ranges. However, such good agreements are obtained at the expense of the discrepancy in total gas mass flow rate. The values of calculated gas products are greater than the measured values at the elevated operating pressures due to overestimation on Char gasification reactions. This significant discrepancy between the calculated values and the experimental data at elevated pressures is shown in Figure 9. The measured data of total gas mass flow rate came from Lin's experiments.[41] The gases include H_2, CH_4, C_2H_6, C_2H_4, CO, and CO_2. But it can be noted that the calculated values are of the same order of magnitude as the experimental data and they have the same trend with increasing operating pressure. Especially at the atmospheric conditions, the total gas mass flow rate is in accord with each other. This is because the kinetic parameters of Char gasification reactions came from atmospheric experiments. It indicates that the reaction parameters selected from the different experimental conditions should be corrected to fit the requirement of the innovative process. It can be concluded that CO_2 absorption is a key process to push water-gas shift reaction forward and higher concentration of Hydrogen is favored in this synergistic process.

Figure 10 shows the prediction of coal conversion profile along the reactor height at the different operating pressures. The prediction of coal conversion has been corrected by the Lin's experiments.[42] In the Lin's experiments, the coal residuals were sampled from the inside of gasifier after the experiment had been finished in steady at the operating pressure of 5.0 MPa and temperature of 923 K. The coal sampling was analyzed by the Thermogravimetric Analysis (TGA), and the measured coal conversion was 81%. According to this experimental datum, the adjusted frequency factors and effectiveness factors, as was mentioned earlier, are also taken into account to improve the simulation. As shown in Figure 10, the calculated coal conversions increase from the bottom to the top of the gasifier. At the operating pressures of 0.1 MPa and 1 MPa, the slight changes of coal conversion along the reactor height can be observed. As the operating pressure varies from 1.0 to 3.0 MPa, a substantial increase of coal conversion occurs at the height range of 0.4–1.0 m. It can be concluded that the gasification rate is significantly accelerated by progressively higher pressure and the coal conversion increases by increasing the operating pressure. The significant influence of pressure on the coal conversion reported by Liu and Niksa[65] is another evidence for this trend.

Prediction of entrained flow coal gasifier

Core-annular structure is one of the main features of the gas-solid flow pattern in the vertical pipe. It was even observed in the risers of oil industry by using gamma ray techniques: the core is very dilute. Two main problems occur in the operation: (1) inefficient gas-solids contacts, (2) back mixing due to nonuniform radial distributions.[24] Figure 11 visualizes the effect of core-annular flow regime on the heterogeneous reaction-Char and H_2O. Figure 11A shows the solid volume fraction of Tartan's riser, and Figure 11B shows the solid volume fraction of Lin's riser. The Char-H_2O reaction rate of Lin's riser is shown in Figure 11C. There are slight difference between the contour of Figure 11A and that of Figure 11B. The main difference is that the core diameter of Tartan's riser is greater than that of Lin's gasifier. It is probably due to their different particulate sizes. According to Geldart classification, Geldart B particles were used in Tartan's riser, and Geldart A particles were used in Lin's gasifier. Gidaspow[68] presented an approximate analyti-

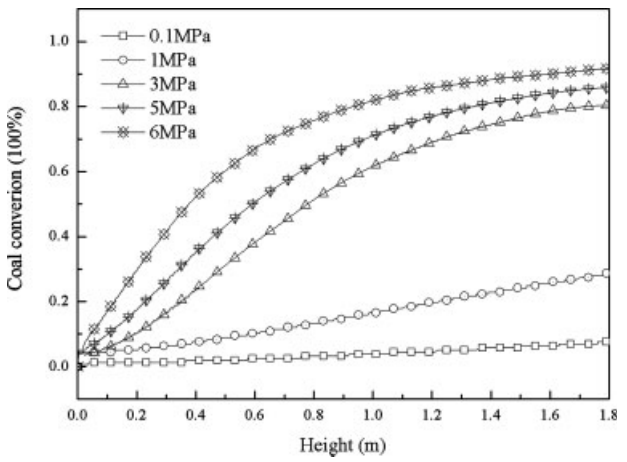

Figure 10. Prediction of coal conversion profile along the reactor height at different operating pressures.

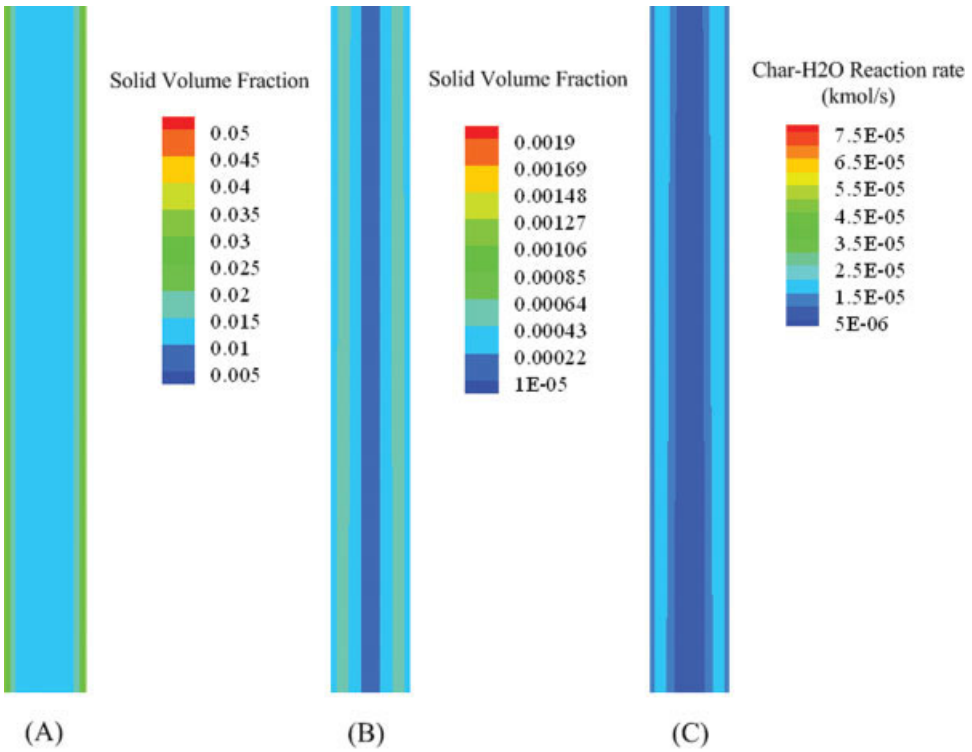

Figure 11. Core-annular flow regime (A) solid volume fraction of Tartan's riser; (B) solid volume fraction of Lin's gasifier; (C) Char-H2O reaction rate of Lin's gasifier.

[Color figure can be viewed in the online issue, which is available at www.interscience.wiley.com.]

cal expression for the maximum carrying capacity of Geldart A, B, and C particles. The expression suggests that for a given gas velocity, the granular temperature should be the highest for Geldart A particles, this means that particles collision is the most intensive for Geldart A particles. Collided with the wall, Geldart A particles are forced near to the core. Besides the effect of particles collision, the solid feed rate of Lin's gasifier is also lower than that of Tartan's riser. Therefore, the solid loading in Lin's gasifier is lower and the core diameter is smaller. Because of the effect of core-annular flow structure, the heterogeneous reaction rate is higher in annular dense solid phase and lower in core dilute solid phase.

Figure 12 visualizes the relationship between velocity and temperature at the Lin's gasifier entrance. Figure 12A shows the contour of gas velocity. When the gasifying agent is injected into the gasifier from the bottom at high speed, they are subject to great resistances such as gravity and solid drag and the gas velocity rapidly decreases. Gradually this jet flow goes in steady. Then the contour of gas velocity looks like a flame shape. The similar shapes are shown in Figures 12B–D for the contours of gas temperature, solid velocity and solid temperature respectively. In the entrance, the gas temperature of 868 K is much higher than the solid temperature of 300 K. Therefore, the gas temperature abruptly decreases first, then increases from the bottom to the top of gasifier due to exothermic heating of CaO hydrate reaction and external heating, while the solid temperature substantially increases due to gas-solid heat transfer.

Figure 13A shows axial gas temperature profile at the different operating pressures and Figure 13B shows axial gas temperature profile at the different radial positions. When the gasifying agent is feed into the reactor at the bottom, an

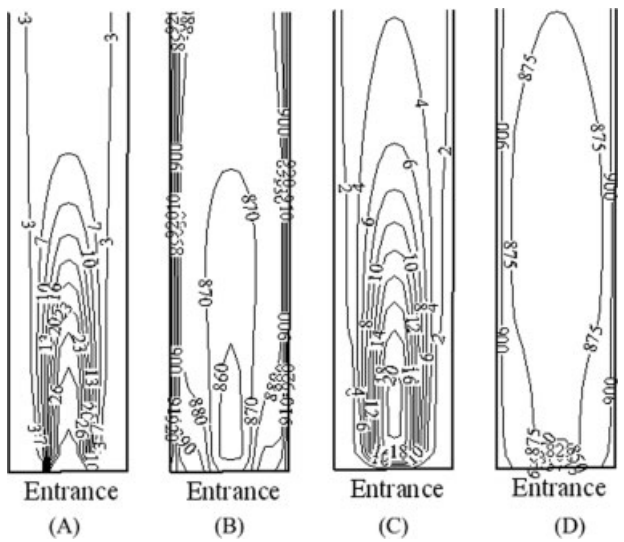

Figure 12. Relationship between velocity and temperature at the entrance (A) gas velocity (B) gas temperature (C) solid velocity (D) solid temperature.

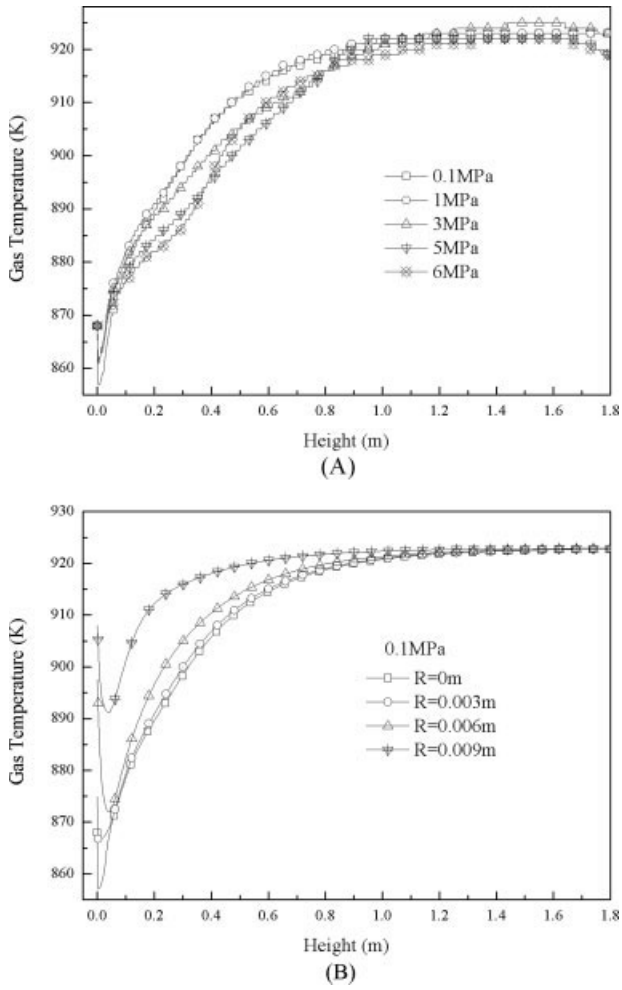

Figure 13. Axial distribution of gas temperature at different operating pressures (A) and different radial positions (B).

abruptly decrease in gas temperature is observed in the axial distribution of gas temperature due to the endothermic volatile (pyrolysis) and coal particles (low temperature). Then the heat from CaO exothermic reaction and external furnace forces the gasifying agent to rise its temperature close to 923 K. As shown in Figure 13A, the gas temperature is reduced with an increase in the system pressure at temperature-rise period. This is attributed to the enhanced endothermic char gasification reactions. However, this trend is not apparent. This is because rapid heats transfer occurs in small bed diameter and CaO exothermic reaction is enhanced by the increasing operating pressure. The heat from CaO exothermic reaction and external furnace can compensate the loss of the enhanced endothermic heat right away. Moreover, as can be seen from 13(B), the gas temperature is lower in the centre of pipe than near wall. It indicates that the overall reaction of single-step hydrogen production is endothermic and a little external heat need to be supplied.

Figure 14 shows concentration profile of gas composition along the reactor height at the different operating pressures. At the operating pressure of 0.1 MPa, CO_2 is not absorbed well by CaO and $Ca(OH)_2$. The effect of gas-water shift reaction is not significant. Therefore, the yield of H_2 is relatively low.[41] With an increase in the operating pressure, CO_2 absorption by CaO and $Ca(OH)_2$ is improved. As shown in Figure 14, the concentration of CO_2 slightly increases first, and then decreases along the reactor height at the operating pressures of 1 and 3 MPa while at the operating pressures of 5 and 6 MPa, CO_2 is absorbed by CaO and $Ca(OH)_2$ as soon as it is created. The concentration of CO is affected by gas-water shift reaction and decreases approximately to zero at the elevated operating pressure. Because of the synergistic effects of CO_2 absorption and gas-water shift reaction, higher concentration of clean hydrogen is produced. Although, CaO is also consumed by H_2S, it has no influence on CO_2 capture and H_2 production due to excessive CaO supplied in the one-step hydrogen production gasifier. The results of reaction of CaO with H_2S in R10 are shown in Figure 15. It can be seen that the sulfidation of CaO increases with increasing operating pressure. In this study, H_2S partial pressure is proportional to operating pressure. The same trend is reported by Chauk et al.[66] However, the sulfidation conversion doesn't take into account CaO sorbent morphological alterations, such as reduction in surface area and pore volume, the effect of total pressure might not be fully predicted.

Figure 16 shows the concentration profile of solid composition along the reactor height at the different operating pressures. In the experiment of single-step hydrogen production, Lin et al.[42] drew a conclusion that the reaction rates decrease in the order CaO hydration $>$ coal pyrolysis $>$ CO_2 absorption by CaO or $Ca(OH)_2$. The thermodynamic analysis results for the explanation of the experimental behaviors illustrated that CaO is first converted into $Ca(OH)_2$ at the reactor entrance. Then $Ca(OH)_2$ is transformed into $CaCO_3$ by CO_2 absorption, where CO_2 is generated by coal gasification. These experimental phenomena can be demonstrated in Figure 16. The concentration of $Ca(OH)_2$ increases abruptly, then has a steep decrease along the reactor height while the concentration of CaO decreases steeply, then gradually increases correspondingly. The rapid drop of the $Ca(OH)_2$ mass fraction is caused by $Ca(OH)_2$ decomposition at higher temperature of 853 K and CO_2 absorption. However, $CaCO_3$ can't be decomposed at the reactor temperature of 923 K due to its higher decomposition temperature. Therefore, $CaCO_3$ is increasingly created by the reaction of CO_2 with CaO/$Ca(OH)_2$ at the elevated temperatures. At the exit of gasifier, the mass fraction of $CaCO_3$ decreases due to a decrease in temperature. This trend is in accord with Lee's experiment.[60] It can also be seen that the higher pressure favors the CaO-carbonation reaction and the mass fraction of $CaCO_3$ increases by increasing operating pressure.

The change in the amount of tar content along the reactor height predicted by the model is shown in Figure 17. As it shows, a steep increase in tar species is initiated from the entrance of gasifier due to pyrolysis of the Volatile. When the amount of tar content reaches a peak, it decreases due to more tar cracking. Apparently, with increasing operating pressure, tar is cracked more significantly, resulting in increased yields of Char and light hydrocarbon gases. This figure demonstrates the importance of pressure in tar removal. The effect of pressure on tar production was also reported by Lin et al.[41] In their experimentation, the tar was found to block the exhaust line at the atmospheric pressure

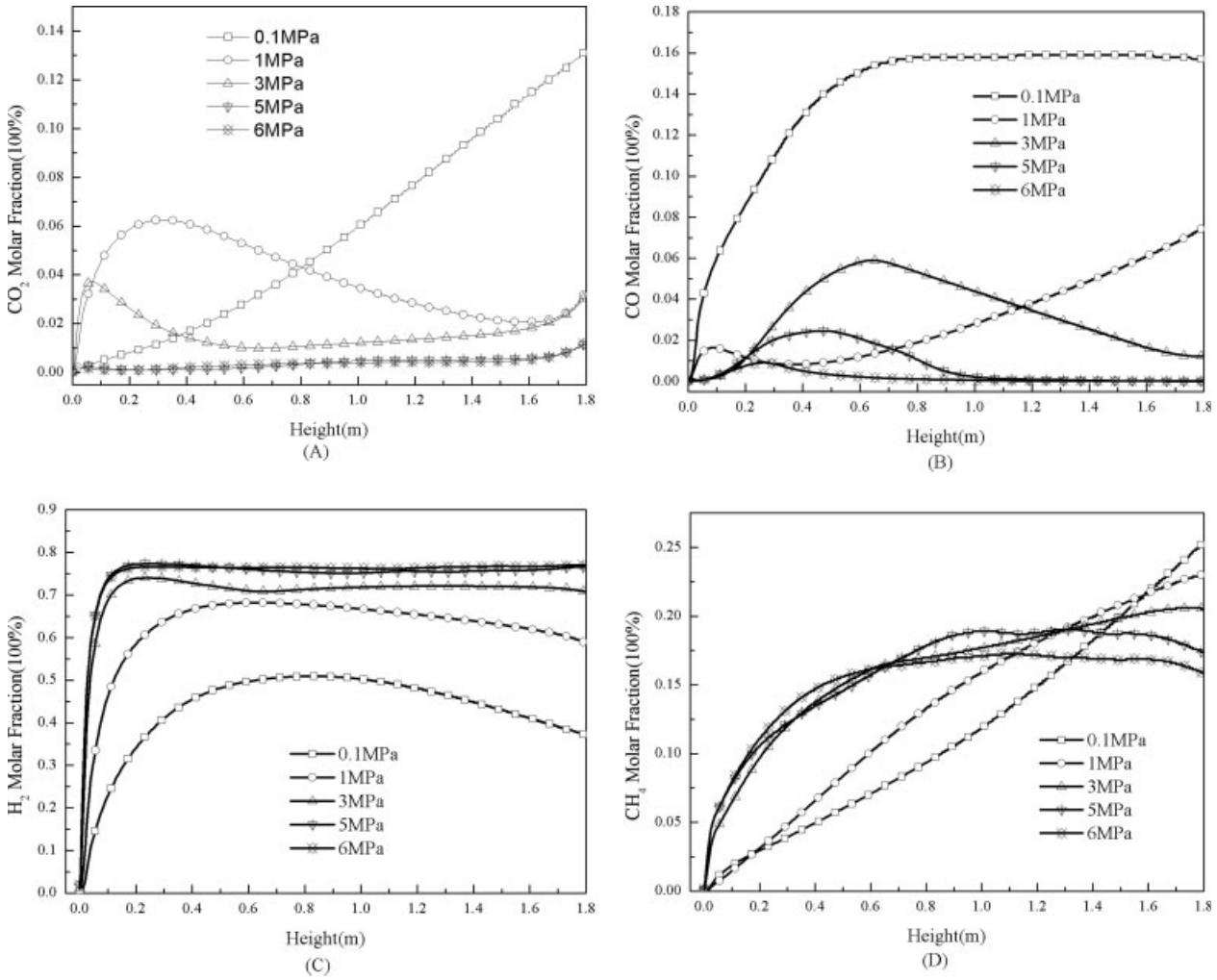

Figure 14. Concentration profile of gas composition along the reactor height at different operating pressures.

and the continuous experiment could be running at the elevated pressures. Wall et al.[67] reported the same trend of tar yields changes with pressure in a coal gasifier. Although Lin et al.[47] reported the amounts of tar are reduced by CaO addition, the effect of CaO addition is not as significantly as that of pressure. Moreover, the mechanism of tar decomposition catalyzed by $CaO/CaCO_3$ is complicated. In this study, this reaction mechanism is simplified and the mass fraction of $CaO/CaCO_3$ is used to accelerate the tar decomposition rate.

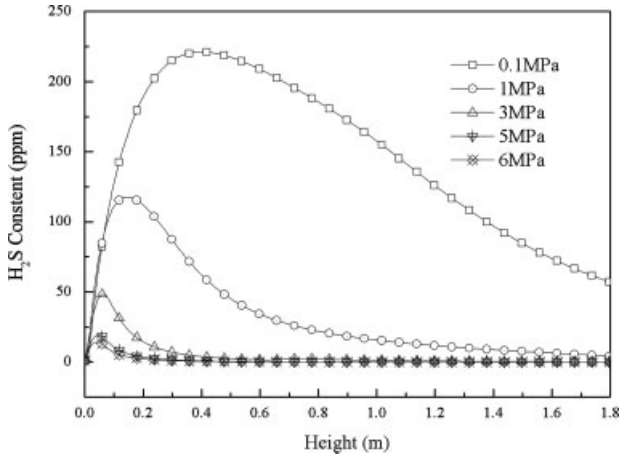

Figure 15. Profile of H_2S content along the reactor height at different operating pressures.

Conclusions

A gas-solid model using kinetic theory was developed to simulate the process of hydrogen production in an entrained flow gasifier. The novel process of hydrogen production was successfully achieved in one reactor by integrating gas production and separation, and the associated endothermic and exothermic reactions. An extended Multi-species of Solid Phase (MSP) method was proposed to deal with many different gas-solid reactions. The intrinsic rate equations were used for the steam reforming of methane, accompanied by water-gas shift reaction, which can reveal the mechanism of high concentration of hydrogen production. The pollutants fixation of CaO was taken into account by the MSP method. It is shown that the characteristic of gas-solid heterogeneous reaction zone is formed like core-annular structure at the fully developed section of the vertical pipe. The feed injection

zone at the bottom of gasifier is the most complex part, where the contour of gas velocity is shown like flame shape, and the gas temperature distribution is correlative to reveal the similar pattern. Higher pressure is very helpful for the absorption of CO_2 by the CaO to drive the equilibrium of water-gas shift reaction forward to produce high-purity hydrogen. The entrained flow gasifier model also showed good agreement with experiments on solid velocity, solid volume fraction, granular temperature, solid viscosity, and the concentration of exit components.

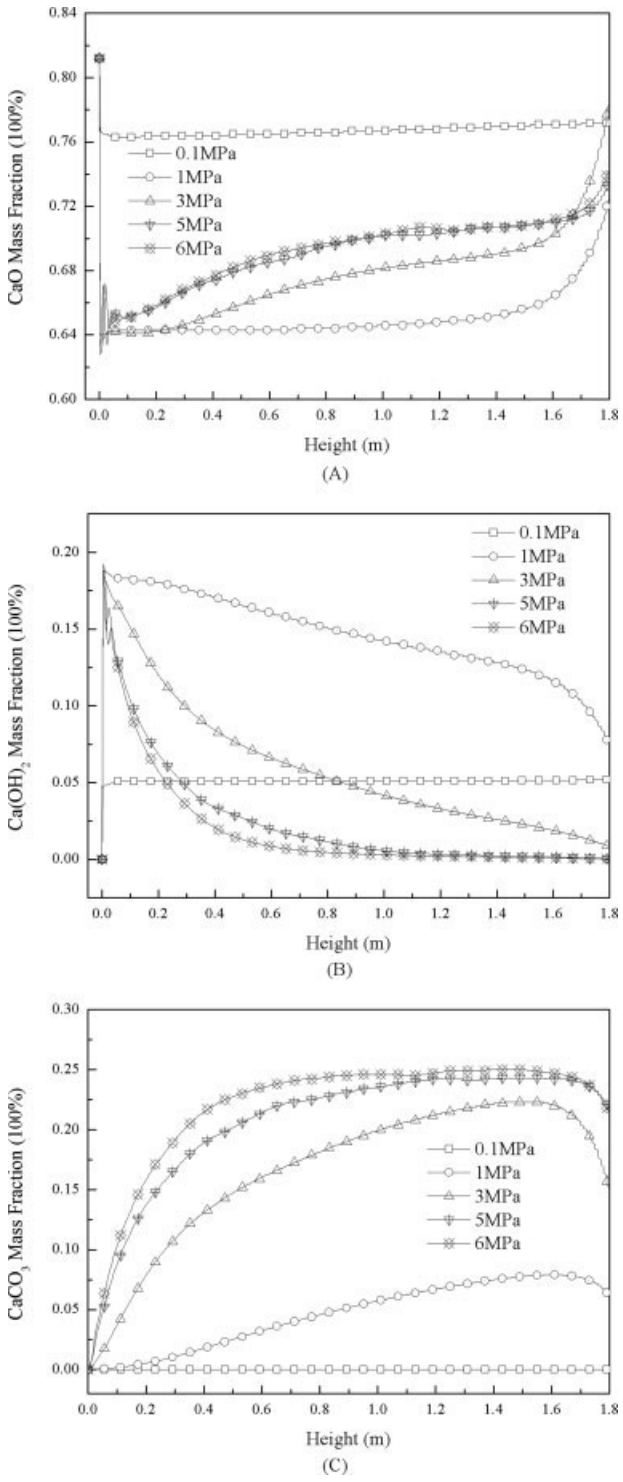

Figure 16. Concentration profile of solid composition along the reactor height at different operating pressures.

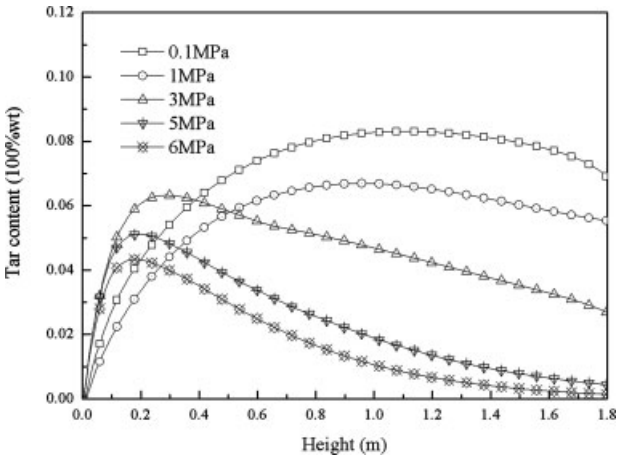

Figure 17. Profile of tar content along the reactor height at different operating pressures.

Future work will address the needs for making a reaction model of no adjustable parameters for one-step hydrogen production. Although the presented model here has proved capable of quantitative prediction of Lin's gasifier, it is not convenient for industrial application due to excessive adjustable parameters. Therefore, a tremendous amount of experimental and modeling works should be done to reveal the quantitative relationship between Char and $CaO/Ca(OH)_2$, and the influence of pressure on gasification mechanism.

Acknowledgments

This work was financially supported by the National Science Fund of China for Distinguished Young Scholars (ProjectNo. 20625618), National Natural Scientific Funding of China (No. 20436050), General Program of the National Natural Science Foundation of China (Project No. 20676135), the 863 Project of China (Project No. 2006AA06Z376) and the Program of Instrument and Equipment Development of Chinese Academy of Sciences (No. Y2005013).

Notation

C = concentration
$C_{p,i}$ = heat capacity, J/kg K
C_d = drag coefficient
$D_{m,i}$ = diffusion coefficient of the mixture, m^2/s
$D_{i,j}$ = binary mass diffusion coefficient, m^2/s
e = coefficient of restitution
g = gravity, m/s^2
g_0 = radial distribution function
H = specific enthalpy, J/kg
H_i = enthalpy, J/kg
$\triangle H_{f,i}$ = enthalpy of formation, J/kg
h_{gs} = heat transfer coefficient, W/m^2 K
$J_{g,i}$ = diffusion flux, kg/m^2 s
K_{Ar} = kinetic rate constant
K_{EBU} = turbulent mixing rate constant
K_{Hom} = homogeneous rate constant
k_s = diffusion coefficient for granular energy, kg/m s
Nu = Nusselt number
$P_{k,g}$ = shear production

Pr = the continuous phase Prandtl number
p = gas pressure, Pa
Q = intensity of heat exchange between the gas and solid phases, W/m^2
R = universal gas constant, J/kmol K
Re = Reynolds number
$R_{g,i}$ = net rate of production of homogeneous species i
$R_{s,i}$ = the heterogeneous reaction rate
r = volume fraction
S = source term
Sh = Shawood number
$S_{P,j}$ = associated stoichiometric coefficients of products
$S_{R,i}$ = associated stoichiometric coefficients of reactants
T = gas mixture mean temperature, K
T_0 = reference temperature, K
U = the instantaneous velocity, m/s
u = the mean velocity, m/s
u' = the fluctuating velocity, m/s
w_i = molecular weight, kg/kmol
X_i = molar fraction
Y_i = the mass fraction

Greek letters

α = mixture thermal conductivity, W/m K
γ = dissipation of fluctuating energy, W/m^3
η = the effectiveness factor
Θ_s = granular temperature, (m/s)^2
λ_s = bulk viscosity, Pa s
μ = viscosity, kg/m s
ρ = density, kg/m^3
τ = stress tensor, Pa
Φ_{gs} = drag, kg/m^3 s

Subscripts

g = gas phase
i = the ith species
m = mixture
s = solid phase

Literature Cited

1. Stiegel GJ, Ramezan M. Hydrogen from coal gasification: an economical pathway to a sustainable energy future. *J Coal Geol*. 2006;65:173–190.
2. Wang J. *Experimental study of coal topping process in a downer reactor. PhD Dissertation*. Beijing: Institute of Process Engineering, Chinese Academy of Sciences, 2005.
3. Lin S, Harada M, Suzuki Y, Hatano H. Comparison of pyrolysis products between coal, coal/CaO, and Coal/Ca(OH)2 materials energy? *Fuels*. 2003;17:602–607.
4. Mondal K, Piotrowski K, Dasgupta D, Hippo E, Wiltowski T. Hydrogen from coal in a single step. *Ind Eng Chem Res*. 2005;44:5508–5517.
5. Asadullah M, Ito S, Kunimori K, Yamada M, Tomishige K. Biomass gasification to hydrogen and syngas at low temperature: novel catalytic system using fluidized-bed reactor. *J Catal*. 2002;208:255–259.
6. Demirbas A. Gaseous products from biomass by pyrolysis and gasification: effects of catalyst on hydrogen yield. *Energy Conversion Manage*. 2002;43:897–909.
7. Rapagna S, Provendier H, Petit C, Kiennemann A, Foscolo PU. Development of catalysts suitable for hydrogen or syn-gas production from biomass gasification. *Biomass Bioenergy*. 2002;22:377–388.
8. Vamvuka D, Woodburn ET, Senior PR. Modelling of an entrained flow coal gasifier. I. Development of the model and general predictions. *Fuel*. 1995;74:1452–1460.
9. Vamvuka D, Woodburn ET, Senior PR. Modelling of an entrained flow coal gasifier. II. Effect of operating conditions on reactor performance. *Fuel*. 1995;74:1461–1465.
10. Liu G, Rezaei HR, Lucas JA, Harris DJ, Wall TF. Modelling of a pressurised entrained flow coal gasifier: the effect of reaction kinetics and char structure. *Fuel*. 2000;79:1767–1779.
11. Fang Y, Huang J, Wang Y, Zhang B. Experiment and mathematical modeling of a bench-scale circulating fluidized bed gasifier. *Fuel Process Technol*. 2001;69:29–44.
12. Brown BW, Smoot LD. Measurement and prediction of entrained-flow gasification processes. *AIChE J*. 1988;34:435–446.
13. Lindsay JD, Paul O. Hedman, Smith PJ. Laser-doppler velocimeter measurements in simulated entrained gasifier flows *AIChE J*. 1989;35:1304–1314.
14. Choi YC, Li XY, Park TJ, Kim JH, Lee JG. Numerical study on the coal gasification characteristics in an entrained flow coal gasifier. *Fuel*. 2001;80:2193–2201.
15. Chen C, Horio M, Kojima T. Numerical simulation of entrained flow coal gasifiers. Part I: modeling of coal gasification in an entrained flow gasifier. *Chem Eng Sci*. 2000;55:3861–3874.
16. Chen C, Horio M, Kojima T. Numerical simulation of entrained flow coal gasifiers. Part II: effects of operating conditions on gasifier performance. *Chem Eng Sci*. 2000;55:3875–3883.
17. Watanabe H, Otaka M. Numerical simulation of coal gasification in entrained flow coal gasifier. *Fuel*. 2006;85:1935–1943.
18. van Wachem BGM, Schouten JC, van den Bleek CM, Krishna R, Sinclair JL. CFD modeling of gas-fluidized beds with a bimodal particle mixture. *AIChE J*. 2001;47:1292–1302.
19. van Wachem BGM, Schouten JC, van den Bleek CM, Krishna R, Sinclair JL. Comparative analysis of CFD models of dense gas-solid systems. *AIChE J*. 2001;47:1035–1051.
20. Patil DJ, van Sint Annaland M, Kuipers JAM. Critical comparison of hydrodynamic models for gas-solid fluidized beds, Part I: Bubbling gas-solid fluidized beds operated with a jet. *Chem Eng Sci*. 2005;60:57–72.
21. Govind R, Shah J. Modeling and simulation of an entrained flow coal gasifier. *AIChE J*. 1984;30:79–92.
22. Arastoopour H, Gidaspow D. Vertical pneumatic conveying using four hydrodynamic models. *Ind Eng Chem Fundam*. 1979;18:123.
23. Vicente W, Ochoa S, Aguillon J, Barrios E. An Eulerian model for the simulation of an entrained flow coal gasifier. *Appl Therm Eng*. 2003;23:1993–2008.
24. Neri A, Gidaspow D. Riser Hydrodynamics: simulation using kinetic theory. *AIChE J*. 2000;46:52–67.
25. Gao J, Xu C, Lin S, Yang G, Guo Y. Advanced model for turbulent gas-solid flow and reaction in FCC riser reactors. *AIChE J*. 1999;45:1095–1113.
26. Gao J, Xu C, Lin S, Yang G, Guo Y. Simulations of gas-liquid-solid 3-phase flow and reaction in fcc riser reactors. *AIChE J*. 2001;47:677–692.
27. He Y, Lu H, Sun Q, Yang L, Zhao Y, Dimitri G, Jacques B. Hydrodynamics of gas-solid flow around immersed tubes in bubbling fluidized beds. *Powder Technol*. 2004;145:88–105.
28. Sinclair JL, Jackson R. Gas-Particle Flow in a vertical pipe with particle-particle interactions. *AIChE J*. 1989;35:1473–1486.
29. Gidaspow D, Jung J, Singh RK. Hydrodynamics of fluidization using kinetic theory: an emerging paradigm: 2002 Flour-Daniel lecture. *Powder Technol*. 2004;148:123–141.
30. Gidaspow D, Lu H. Equation of state and radial distribution functions of fcc particles in a CFB. *AIChE J*. 1998;44:279–293.
31. Mathiesen VTS, Arastoopour H, Hjertager BH. Experimental and computational study of multiphase gas/particle flow in a cfb riser. *AIChE J*. 1999;45:2503–2518.
32. Iddir H, Arastoopour H. Modeling of multitype particle flow using the kinetic theory approach. *AIChE J*. 2005;51:1620–1632.
33. Colomba Di B. Modeling wood gasification in a countercurrent fixed-bed reactor. *AIChE J*. 2004;50:2306–2319.
34. Corella J, Sanz A. Modeling circulating fluidized bed biomass gasifiers: a pseudo-rigorous model for stationary state. *Fuel Process Technol*. 2005;86:1021–1053.
35. Radmanesh R, Chaouki J, Guy C. Biomass gasification in a bubbling fluidized bed reactor: experiments and modeling. *AIChE J*. 2006;52:4258–4272.
36. Neogi D, Chang CC, Walawender WP, Fan LT. Study of coal gasification in an experimental fluidized bed reactor. *AIChE J*. 1986;32:17–28.
37. Yan HM, Heidenreich C, Zhang DK. Modelling of bubbling fluidised bed coal gasifiers. *Fuel*. 1999;78:1027–1047.
38. Chejne F, Hernandez JP. Modelling and simulation of coal gasification process in fluidised bed. *Fuel*. 2002;81:1687–1702.

39. Yu L, Lu J, Zhang X, Zhang S. Numerical simulation of the bubbling fluidized bed coal gasification by the kinetic theory of granular flow (KTGF). *Fuel*. 2007;86:722–734.
40. Tartan M, Gidaspow D. Measurement of granular temperature and stresses in risers. *AIChE J*. 2004;50:1760–1775.
41. Lin S, Harada M, Suzuki Y, Hatano H. Continuous experiment regarding hydrogen production by coal/Cao reaction with steam (II) solid formation. *Fuel*. 2006;85:1143–1150.
42. Lin S, Harada M, Suzuki Y, Hatano H. Hydrogen production from coal by separating carbon dioxide during gasification. *Fuel*. 2002;81: 2079–2085.
43. Balasubramanian B, Lopez Ortiz A, Kaytakoglu S, Harrison DP. Hydrogen from methane in a single-step process. *Chem Eng Sci*. 1999;54:3543–3552.
44. Kuramoto K, Furuya T, Suzuki Y, Hatano H, Kumabe K, Yoshiie R, Moritomi H, Shi-Ying L. Coal gasification with a subcritical steam in the presence of a CO2 sorbent: products and conversion under transient heating. *Fuel Process Technol*. 2003;82:61–73.
45. Ohtsuka Y, Tomita A. Calcium Catalysed steam gasification of yallourn brown coal. *Fuel*. 1986;65:1653–1657.
46. Lin S, Suzuki Y, Hatano H, Harada M. Developing an innovative method, *Hypr-RING*, to produce hydrogen from hydrocarbons. *Energy Conversion Manage*. 2002;43:1283–1290.
47. Wang J, Takarada T. Role of calcium hydroxide in supercritical water gasification of low-rank coal. *Energy Fuels*. 2001;15:356–362.
48. Lin S, Harada M, Suzuki Y, Hatano H. Continuous experiment regarding hydrogen production by coal/Cao reaction with steam (I) gas products. *Fuel*. 2004;83:869–874.
49. de Souza-Santos ML. Comprehensive modelling and simulation of fluidized bed boilers and gasifiers. *Fuel*. 1989;68:1507–1521.
50. Eaton AM, Smoot LD, Hill SC, Eatough CN. Components, formulations, solutions, evaluation, and application of comprehensive combustion models. *Prog Energy Comb Sci*. 1999;25:387–436.
51. Breault RW. A review of gas-solid dispersion and mass transfer coefficient correlations in circulating fluidized beds. *Powder Technol*. 2006;163:9–17.
52. Lee DK. An apparent kinetic model for the carbonation of calcium oxide by carbon dioxide. *Chem Eng J*. 2004;100:71–77.
53. Xu J, Froment GF. Methane steam reforming, methanation and water-gas shift: 1 intrinsic kinetics *AIChE J*. 1989;35:88–95.
54. Abashar MEE. Coupling of steam and dry reforming of methane in catalytic fluidized bed membrane reactors. *Int J Hydrogen Energy*. 2004;29:799–808.
55. Hoang DL, Chan SH. Modeling of a catalytic autothermal methane reformer for fuel cell applications. *Appl Catal A: Gen*. 2004;268: 207–216.
56. El-Bousiffi MA, Gunn DJ. A dynamic study of steam-methane reforming. *Int J Heat Mass Transf*. 2007;50:723–733.
57. Chen R, Chen Z. Study on the hydration kinetics of free CaO in high calcium fly ash. *J Build Mater*. 2000;3:147–150.
58. Zhong Z, Mamie T, Jin B, Zhou H and Cai N. Study on Desulfurization in Pressure and Reducing Atmosphere. *Energy Res Util*. 2002;20–23.
59. Ding J, Gidaspow D. A Bubbling Fluidization Model Using Kinetic Theory of Granular Flow. *AIChE J*. 1990;36:523–538.
60. Yang YB, Lim CN, Goodfellow J, Sharifi VN, Swithenbank J. A Diffusion Model for Particle Mixing in a Packed Bed of Burning Solids. *Fuel*. 2005;84:213–225.
61. Gunn DJ. Transfer of Heat or Mass to Particles in Fixed and Fluidized Beds. *Int J Heat Mass Transf*. 1978;21:467–476.
62. Louge MY, Bricout V, Martin-Letellier S. On the Dynamics of Pressurized and Atmospheric Circulating Fluidized Bed Risers. *Chem Eng Sci*. 1999;54:1811–1824.
63. Lee DK, Baek IH, Yoon WL. Modeling and Simulation for the Methane Steam Reforming Enhanced by in situ CO2 Removal Utilizing the CaO Carbonation for H2 Production. *Chem Eng Sci*. 2004;59:931–942.
64. de Groote AM, Froment GF. Simulation of the Catalytic Partial Oxidation of Methane to Synthesis Gas. *Appl Catal A: Gen*. 1996;138: 245–264.
65. Liu G, Niksa S. Coal Conversion Submodels for Design Applications at Elevated Pressures. Part II. Char gasification. *Prog Energy Comb Sci*. 2004;30:679–717.
66. Shriniwas S, Chauk R, Jadhav ARA, Misro SK, Fan LS. Kinetics of high-pressure removal of hydrogen sulfide using calcium oxide powder. *AIChE J*. 2000;46:1157–1167.
67. Wall TF, Liu G, Wu H, Roberts DG, Benfell KE, Gupta S, Lucas JA, Harris DJ. The effects of pressure on coal reactions during pulverised coal combustion and gasification. *Prog Energy Comb Sci*. 2002;28:405–433.
68. Gidaspow D, Reza M. Maximum Carrying Capacity and Granular Temperature of A, B and C Particles. *AIChE J*. 2003;49:831–843.

Manuscript received Dec. 11, 2007, revision received Mar. 17, 2008, and revision received July 10, 2008.